Global and diurnal variations in tropospheric ammonia observed from a constellation of hyperspectral infrared sounders in three different LEO orbits

Jiancong Hua[1], Runyi Zhou[1], Mengya Sheng[1], Zhao-Cheng Zeng[1]

[1]School of Earth and Space Sciences, Peking University, Beijing 100087, China

Correspondence to: Zhao-Cheng Zeng (zczeng@pku.edu.cn)

Abstract. As a reactive nitrogen compound, atmospheric ammonia (NH_3) plays a key role in the global nitrogen cycle. Tracking the spatiotemporal dynamics of NH_3 is crucial to quantify its emissions and depositions, as well as offering insights to inform the regulation of anthropogenic emission sources. Currently, the diurnal cycle of NH_3 remains under-constrained, particularly in regions lacking geostationary satellite observations, which poses a challenge to accurate emission quantification. To address this gap, we construct an integrated constellation to achieve quasi-geostationary-like global monitoring coverage, comprising China's FengYun-3 (FY-3) series satellites and the Cross-track Infrared Sounder (CrIS). FY-3E operates in a dawn-dusk orbit with equatorial overpassing time at 05:30 am/pm, while FY-3F operates in a mid-morning orbit with overpassing time at 10:00 am/pm. Both are equipped with the second-generation High Spectral Infrared Atmospheric Sounder (HIRAS-II). CrIS, operating with overpassing time at 01:30 am/pm, provides supplementary observations in an afternoon orbit. In this study, hyperspectral infrared observations from the constellation are utilized to retrieve global NH_3 columns based on the optimal estimation method. Six maps of global NH_3 for every 4-hour in each day are retrieved. The retrieval results in four weeks of different seasons in 2024, as a demonstration, show elevated columns in global major source regions, including the North China Plain, the Indo-Gangetic Plain, North America and Western Europe. In addition, the diurnal and seasonal cycles of NH_3 over these regions using all observations in 2024 are also investigated. The constellation reasonably captures the diurnal (every 4-hour) and seasonal cycles of NH_3 columns, effectively mitigating the constraints in regions without geostationary observations. Further cross-comparisons with the Geostationary Interferometric Infrared Sounder (GIIRS) retrievals and ground-based Fourier transform infrared spectroscopy (FTIR) measurements demonstrate that the polar-orbiting constellation retrievals are internally consistent and broadly consistent with independent observations, supporting their capability to capture major NH_3 spatial patterns and temporal variability. The sensitivity of NH_3 detection in the lower atmosphere as quantified by the column averaging kernel (AVK) from the retrieval shows diurnal variations that dependent on thermal contrast, defined as the temperature difference between the surface and the lower atmospheric layer. This study demonstrates the capability of the integrated constellation, comprising FY-3E/HIRAS-II (dawn-dusk), FY-3F/HIRAS-II (mid-morning), and CrIS (afternoon), to monitor global and diurnal NH_3 variations at unprecedentedly six distinct times of a day, and has the potential to enhance the global climate-monitoring capacity of polar-orbiting meteorological satellites.

1 Introduction

As a critical reactive nitrogen compound, ammonia (NH_3) holds considerable importance in the atmosphere and global nitrogen cycle, yet it also acts as a hazardous pollutant affecting human health and ecosystems. Specifically, it contributes to smog via its neutralization of sulfuric and nitric acids, resulting in the generation of secondary aerosols including ammonium sulfate and ammonium nitrate. (Galloway et al., 2004; Behera et al., 2013). These particles can travel long distances, degrading air quality and disrupting ecological balance (Erisman et al., 2013). These ammonium-based particles, along with NH_3 itself, can be converted into various reactive nitrogen forms that trigger acid precipitation, eutrophication, and reduced biodiversity (Sutton et al., 2011). Under specific conditions, ammonium nitrate particles may volatilize to reform gaseous NH_3, creating a dynamic cycle that complicates its environmental impacts (Weber et al., 2016; Guo et al., 2018). Agriculture serves as the dominant source, stemming from fertilizer storage, livestock manure, and the application of mineral nitrogen fertilizers to crops (Fowler et al., 2013). Secondary contributors to NH_3 emissions encompass biomass combustion, industrial operations, and automobiles fitted with three-way catalytic converters (Galloway et al., 2003; Erisman et al., 2008). After being emitted into the atmosphere, NH_3 exhibits a brief residence time ranging from several hours to a handful of days, and its primary removal pathways are dry and wet deposition processes (Liu et al., 2013; Dammers et al., 2017; Zhang et al., 2018). These deposition processes accelerate soil acidification, further exacerbating the ecological damage. Beyond air quality and ecosystem impacts, the aerosols derived from NH_3 also influence climate by scattering solar radiation, modifying albedo, and altering the properties of clouds (Adams et al., 2001; Abbatt et al., 2006; Isaksen et al., 2009; Myhre et al., 2013).

Different technologies have been used to monitor atmospheric NH_3. A number of in situ monitoring sites have been established (Jiménez et al., 2015; De Mazière et al., 2018). Moreover, satellites furnished with high-resolution infrared spectrometers have provided unprecedented spatiotemporal sampling of global NH_3 distributions, and this has driven major progress in understanding NH_3 emission and deposition fluxes covering spatial scopes ranging from local-level to global-scale, together with their temporal fluctuation characteristics. Polar-orbiting satellites are capable of delivering global observational coverage up to two times per day, including the Infrared Atmospheric Sounding Interferometers (IASI, e.g., Clarisse et al., 2009) at 09:30/21:30 (Local Solar Time, LST), Tropospheric Emission Spectrometer (TES, e.g., Beer et al., 2008; Shephard et al., 2011), the Atmospheric Infrared Sounder (AIRS, e.g., Warner et al., 2016)) and the Cross-track Infrared Sounder (CrIS, e.g., Shephard and Cady-Pereira, 2015) at 01:30/13:30 LST, the Thermal and Near-infrared Spectrometer for Observation-Fourier Transform Spectrometer (TANSO-FTS; e.g., Someya et al., 2020) at 01:00/13:00 LST and FengYun-3D (FY-3D, e.g. Zhou et al., 2024) at 02:00/14:00 LST. Recently, diurnal variations of atmospheric NH_3 over the Asian region have been observed using the Geostationary Interferometric Infrared Sounder (GIIRS) aboard the FengYun-4A (FY-4A/GIIRS, Clarisse et al., 2021) and FengYun-4B (FY-4B/GIIRS, Zeng et al., 2023; Sheng et al., 2025; Guendouz et al., 2026) satellites. The Infrared Sounder (IRS) aboard the Meteosat Third Generation (MTG), which was launched in 2025, is expected to provide geostationary observations over Europe and Africa (Holmlund et al., 2021; Guendouz et al., 2026). Such geostationary orbit-based monitoring offers significant advantages and potential for investigating NH_3 diurnal variations, which in turn facilitates a deeper understanding of its emission, deposition, transport and other related processes. However, there is currently a lack of geostationary orbit observations across most global regions especially in most of the Southern Hemisphere and North America. Atmospheric NH_3 shows notable spatiotemporal variability, largely attributed to its primary emission characteristics and short atmospheric lifetime. This inherent variability underscores the urgent need for a high-resolution and globally comprehensive monitoring system.

To address this gap, we construct an integrated constellation to achieve quasi-geostationary-like global monitoring coverage, comprising China's FengYun-3 (FY-3) series satellites and CrIS. Similar constellation has been developed for monitoring volcanic sulfur dioxide (Zeng et al., 2025). NH_3 retrievals employing the optimal estimation method, will be conducted under this framework to enable quasi-geostationary observations up to six times a day globally. This work is expected to provide crucial observational data for clarifying global and diurnal NH_3 variations.

The subsequent sections of this paper are organized as follows. Section 2 elaborates on the methodological approaches adopted in the present research. Section 3 presents and discusses the retrieval results from the constellation. Finally, the conclusions are drawn in Section 4.

2 Methodologies

2.1 A constellation of hyperspectral infrared sounders

The High Spectral Infrared Atmospheric Sounder (HIRAS) aboard the FY-3 satellite series is a Fourier Transform Michelson interferometer. It measures upwelling infrared radiative signals across the short-wave, mid-wave, and long-wave infrared bands. HIRAS-II is the second-generation of the HIRAS sensor and is carried onboard both FY-3E and FY-3F, which were successfully launched in 2021 and 2023, respectively (Zhang et al., 2022a, b). FY-3E/HIRAS-II is deployed in a dawn-dusk orbit, with an equatorial overpass time of 05:30 am/pm (Local Solar Time, LST), while FY-3F/HIRAS-II operates in a mid-morning orbit featuring an overpass time of 10:00 am/pm LST. Combined with CrIS aboard the Joint Polar Satellite System-1 (JPSS-1) platform, which has an overpass time of 01:30 am/pm LST, these three sensors form a global constellation observation system (Fig. 1a). Note that IASI's overpass times, approximately 09:30 and 21:30 LST, are close to those of FY-3F/HIRAS-II at 10:00 and 22:00 LST and thus can provide additional mid-morning orbit observations. For this concept study, however, only FY-3F/HIRAS-II is used. Their overpass times are shown in Fig. 1b, and the corresponding histograms are presented in Fig. 1c.

Both HIRAS-II instruments aboard the FY-3E and FY-3F satellites, as well as the CrIS share key technical specifications with a nadir spatial resolution of 14 km and an unapodised spectral resolution of 0.625 cm^{-1} (Zhang et al., 2024). Specifically, HIRAS-II provides continuous spectral coverage across 650–2550 cm^{-1} via 3041 channels, while CrIS matches this spectral resolution, ensuring all three instruments fully cover the characteristic rotational-vibrational ν_2 band of NH_3 centered near 10.5 μm. For NH_3 retrieval, we use the 955–975 cm^{-1} band extracted from observations of all three instruments. No empirical sensor-specific radiometric bias correction or additional spectral harmonization is applied before the retrievals. We randomly select one day of observations from the three satellites over the North China Plain and calculate their spectral noise. The noise equivalent differential temperature (NedT) of HIRAS-II aboard FY-3E and FY-3F is approximately 0.08 K, while that of CrIS is around 0.05 K. These noise levels are of a comparable magnitude and sufficiently sensitive to detect variations in NH_3, ensuring uniform observational quality for cross-instrument analysis (Zavyalov et al., 2013; Shephard and Cady-Pereira, 2015; Zhang et al., 2024). While CrIS already has well-established and mature NH_3 products from the CrIS Fast Physical Retrieval (CFPR) dataset developed by Environment and Climate Change Canada (Shephard et al., 2020), we adopt a unified retrieval algorithm for all three instruments. This choice is driven by the need to ensure consistency across the satellite constellation, enabling direct inter-comparability between FY-3E/HIRAS-II, FY-3F/HIRAS-II, and CrIS observations. For CrIS retrievals, we use JPSS-1 CrIS Level 1B Full Spectral Resolution V3 data as input, maintaining methodological coherence with our processing of HIRAS-II observations.

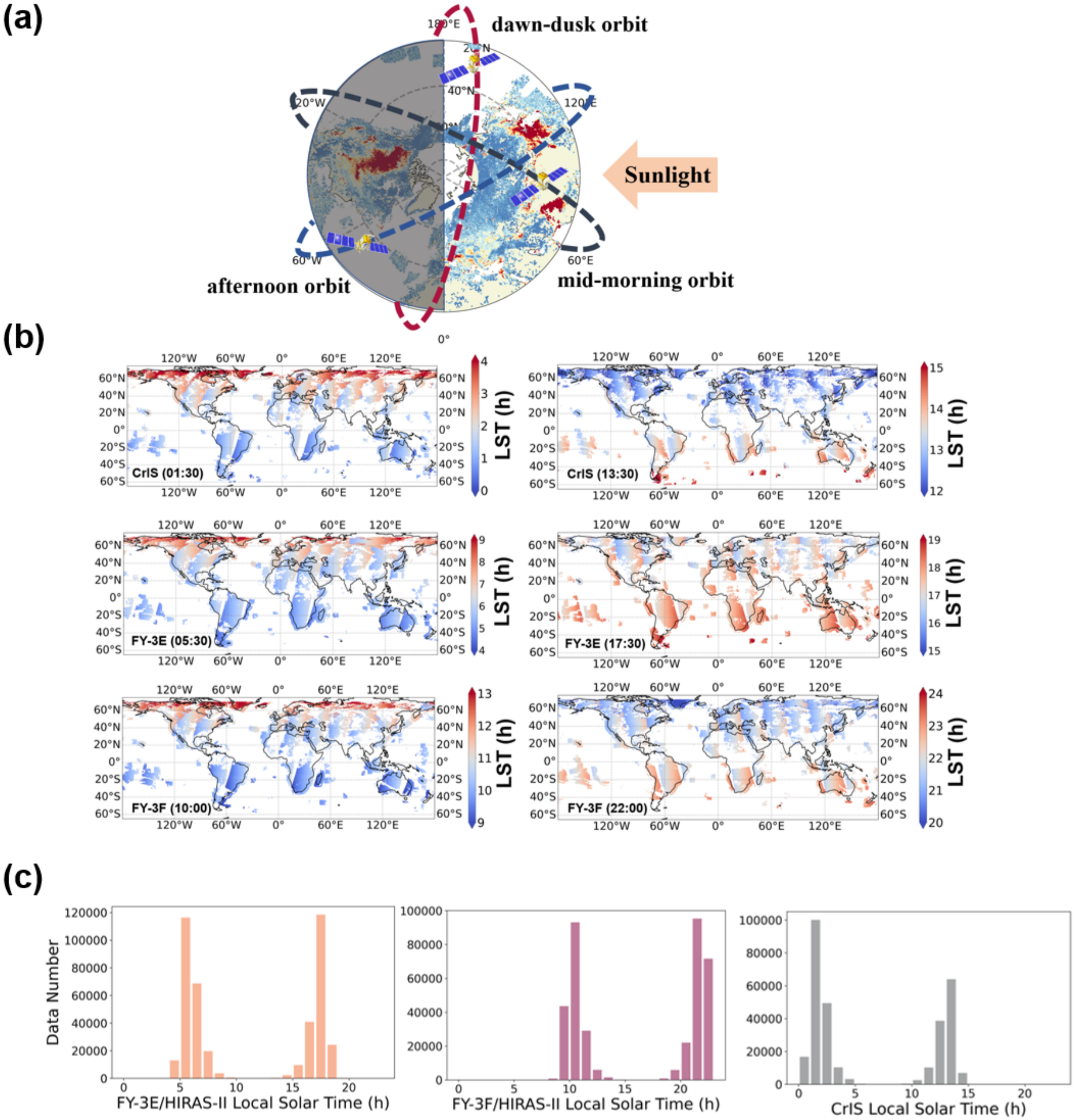

Figure 1. (a) Schematic diagram of three polar-orbiting satellites with different orbits. FY-3E/HIRAS-II operates in a dawn-dusk orbit, with an equatorial overpass time of 05:30 am/pm LST, FY-3F/HIRAS-II is in a mid-morning orbit with an equatorial overpass time of 10:00 am/pm LST, and the CrIS has an equatorial overpass time of 01:30 am/pm LST. The color gradient in the background represents the retrieved global distribution of NH_3 columns on 19 July 2024, as will be discussed in subsequent analyses. (b) Local Solar Time (LST) of observations acquired by FY-3E/HIRAS-II, FY-3F/HIRAS-II and CrIS over terrestrial and offshore regions. Observations over polar areas and remote oceans are excluded. These maps are constructed from cloud-screened observations collected on 19 July, 2024. (c) Histograms of the overpass Local Solar Time (LST) for FY-3E/HIRAS-II, FY-3F/HIRAS-II, and CrIS. Examples are derived from observations taken on 19 July, 2024.

2.2 Optimal estimation methods

For the retrieval, only cloud-screened spectra from FY-3E/HIRAS-II, FY-3F/HIRAS-II, and CrIS are used. To remove cloud-contaminated pixels and ensure consistency across sensors, we apply a unified cloud-screening procedure following the brightness-temperature-difference method of Wells et al. (2020, 2022). Specifically, for each observation, the observed brightness temperature near 900 cm^{-1} is compared with the nearest-hourly ERA5 surface skin temperature. The cloud-screening threshold is adjusted according to the ERA5 water vapor column, and no fixed cloud-fraction threshold is used. Observations for which the 900 cm^{-1} brightness temperature is lower than this water-vapor-dependent threshold relative to the surface skin temperature are flagged as cloud-contaminated and excluded. The same cloud-screening procedure is applied to FY-3E/HIRAS-II, FY-3F/HIRAS-II, and CrIS to maintain consistency across different satellites.

The NH_3 retrieval is based on the FengYun-Low Earth Orbit Atmospheric Infrared Retrieval algorithm (FY-LeoAIR), which adapts the optimal-estimation framework and forward-model structure of the FY-GeoAIR algorithm originally developed for FY-4B/GIIRS NH_3 retrievals by Zeng et al. (2023). FY-LeoAIR has previously been applied to trace gas retrievals from FY-3E/HIRAS-II observations, including CO and VOCs (e.g., Zeng, 2025; Hua et al., 2025). In this study, FY-LeoAIR is extended to global NH_3 retrievals from FY-3E/HIRAS-II, FY-3F/HIRAS-II, and CrIS.

The retrieval is performed in the 955–975 cm^{-1} band, which contains strong NH_3 absorption features and is fully covered by all three sensors. Sensor-specific spectral noise estimates are used to construct the diagonal measurement-error covariance matrix. The same forward model, retrieval method, and quality-control procedure are used for all three sensors to maintain internal consistency.

FY-LeoAIR combines a clear-sky infrared radiative transfer forward model with an optimal-estimation-based inverse model. The forward model uses atmospheric temperature, H_2O, O_3, and surface pressure from ERA5, CO_2 from ECMWF CAMS greenhouse-gas products, and other weakly interfering trace-gas profiles from standard atmospheric profiles, following the configuration of Zeng et al. (2023). Surface skin temperature is initialized from ERA5 and retrieved simultaneously with the trace gases. The a priori land surface emissivity used in the forward model is taken from the University of Wisconsin-Madison global infrared land surface emissivity database (UOW-M), as in Zeng et al. (2023). The a priori surface emissivity spectrum is adjusted within the retrieval window using a fourth-order Legendre polynomial expansion, with the first- to fourth-order coefficients retrieved simultaneously. The parameters in the retrieval state vector are summarized in Table S1.

The main modification relative to Zeng et al. (2023) is that NH_3 is retrieved using a single multiplicative profile-scaling factor applied to a fixed a priori NH_3 profile, rather than as independent layer-by-layer NH_3 elements. The same profile-scaling strategy is also applied to H_2O in this implementation. This approach is adopted because the NH_3 information content in individual thermal infrared observations is generally limited, with the degree of freedom for signal mostly below 1, making independent layer-resolved retrievals insufficiently constrained for global multi-sensor processing. The profile-scaling approach also improves computational efficiency for the global constellation retrieval. Similar retrieval strategy has also been adopted by FY-4B/GIIRS NH_3 retrievals (Sheng et al., 2025).

The fixed NH_3 a priori profile is constructed following Zeng et al. (2023), based on GEOS-CF NH_3 simulations over representative polluted land regions in East Asia and South Asia. The same normalized profile shape is used for all retrievals, while the retrieved scaling factor determines the retrieved NH_3 abundance. This choice helps avoid introducing artificial spatial or temporal variability from a time-varying prior into the retrieved columns. Retrieval uncertainty and the column averaging kernel are used to characterize the information content of each retrieval. We also conduct an a priori profile sensitivity test (see Text S1 and Figs. S1-S6 in the supplementary material).

Because NH_3 is mainly concentrated in the lower troposphere, the retrieval state vector only adjusts NH_3 in 11 atmospheric layers from the surface to 200 hPa. The reported NH_3 total column is calculated as the sum of the retrieved surface-to-200 hPa NH_3 column and the fixed a priori contribution above 200 hPa. Since the NH_3 abundance above 200 hPa is generally small and is not independently constrained by the spectra, the spatial and temporal variability discussed in this study is dominated by the retrieved surface-to-200 hPa component.

An optimal state vector for minimizing discrepancies between forward model-simulated spectra and sensor-measured spectra is derived by the optimal estimation framework. In practice, the retrieval algorithm outputs the state vector that minimizes the cost function defined as:

$$J(\boldsymbol{x}) = \chi^2 = [\boldsymbol{y} - \mathbf{F}(\boldsymbol{x}, \boldsymbol{b})]^T \boldsymbol{S_\varepsilon}^{-1} [\boldsymbol{y} - \mathbf{F}(\boldsymbol{x}, \boldsymbol{b})] + (\boldsymbol{x} - \boldsymbol{x_a})^T \boldsymbol{S_a}^{-1} (\boldsymbol{x} - \boldsymbol{x_a}) \,, \tag{1}$$

Here, $\boldsymbol{y}$ denotes the satellites measured radiance within the NH_3 retrieval band. $\mathbf{F}$ is the forward model that produces simulated radiance for the retrieval process. $\boldsymbol{x}$ is the retrieval state vector, including the NH_3 profile-scaling factor, the H_2O profile-scaling factor, scaling factors for interfering trace gases, surface skin temperature, atmospheric temperature scaling, and four surface-emissivity Legendre polynomial coefficients. $\boldsymbol{x_a}$ denotes the a priori vector. $\boldsymbol{b}$ stands for a set of fixed non-retrieved auxiliary parameters. $\boldsymbol{S_a}$ is the a priori covariance matrix corresponding to the state vector. $\boldsymbol{S_\varepsilon}$ represents the measurement error covariance matrix, treated as a diagonal matrix derived from spectral noise estimates. Retrieval outputs include the NH_3 column, posteriori column retrieval uncertainty estimation, and column averaging kernel (AVK). The column AVK quantitatively represents the response of total NH_3 column to variations in the partial column at each layer, which is important for cross-comparison and model assimilation of satellite retrievals. A more detailed description of column AVK is provided in (Sheng et al., 2025).

3 Results and Discussions

3.1 Global variations of NH_3 columns from the LEO constellation

As an illustrative demonstration of the global sampling capability of the LEO constellation, we first examine representative seven-day mean NH_3 column distributions in January, April, July, and October 2024, specifically January 12–18, April 12–18, July 17–23, and October 1–7. These weekly maps are intended to demonstrate the global spatial coverage and broad seasonal contrast captured by the constellation, rather than to provide a climatological seasonal mean. We first retrieve global daily maps of NH_3 columns, re-grid them to a 0.5° × 0.5° spatial resolution, and then calculate seven-day averages for these representative periods. A strict quality control process is applied to ensure the reliability of satellites retrievals. Observations that fail to achieve convergence within 10 iterations are excluded from the dataset. We then implement a series of post-filters, retaining only those retrieval results that satisfy all the following criteria simultaneously. First, the retrieved NH_3 columns are required to be positive. Second, the absolute difference in surface skin temperature between the a priori and retrieved values is less than 10 K. Third, the retrieval error of the column does not exceed 300%. Fourth, the surface AVK is greater than 0.1. Fifth, the absolute thermal contrast (TC), defined as the temperature difference between the surface and the lowest atmospheric layer, is larger than 3 K. The absolute TC > 3 K and surface AVK > 0.1 criteria used here are intended for the global spatial-distribution analysis, where the objective is to illustrate the broad coverage and spatial patterns retrieved by the LEO constellation while retaining sufficient sampling density. These criteria remove retrievals with weak thermal contrast and limited near-surface sensitivity, but they are less restrictive than the criteria used later for the regional hotspot diurnal analysis. The effect of different TC and AVK thresholds on spatial distributions, diurnal cycles, and data retention is further evaluated and presented in the Supplementary Fig. S7-10. Sixth, a threshold for surface emissivity at 8.3 μm is set at 0.9, with only results meeting this threshold retain. This step is designed to avoid the occurrence of abnormally high NH_3 column concentrations over desert regions, consistent with the method of Clarisse et al. (2019). The surface emissivity data used for this filter are obtained from the Combined ASTER and MODIS Emissivity over Land Database Monthly Global 0.05° V003, which provides global monthly emissivity data at a 0.05° spatial resolution.

As shown in Figs. 2 and 3, broad seasonal contrasts in the representative weekly global NH_3 maps are evident across the four selected periods. In January, elevated NH_3 columns are concentrated in the Indo-Gangetic Plain and Central Africa, which is primarily associated with ongoing agricultural activities such as winter fertilizer application and extensive biomass burning for land clearance in these regions. In April, high NH_3 loading persists in the Indo-Gangetic Plain, East China and Central Africa, driven by intensified spring planting and corresponding fertilizer use in agricultural hotspots. Southeast Asia also exhibits increased NH_3 levels during this month, a pattern attributed to widespread slash-and-burn agriculture practices that are common in the regional dry season to prepare farmland. Additionally, scattered high NH_3 columns are observed in parts of North America, likely linked to localized agricultural operations and small-scale biomass burning. In July, high NH_3 columns remain concentrated in the Indo-Gangetic Plain, the North China Plain, Central Africa and Western Europe. The sustained high levels in these areas correlate with summer agricultural activities and elevated temperatures that enhance emissions (Ding et al., 2024). In particular, large-scale wildfires during the summer in North America exert a broad-range impact, leading to significantly elevated NH_3 columns across extensive regions as a result of biomass burning releasing substantial amounts of NH_3 (Lutsch et al., 2019). Within the smoke plumes, rapid gas-particle partitioning of NH_3 and favorable ammonium nitrate formation in cold, high-altitude conditions sustain column enhancements even as the plume disperses, reinforcing the widespread NH_3 elevations we observe (Lindaas et al., 2021). October still sees detectable high NH_3 columns over the Ini Plain, where post-harvest agricultural residues burning and late-season fertilizer application maintain elevated emissions. In South America, elevated NH_3 levels are mostly attributed to combined effects of fertilizer usage for autumn crops and biomass burning, as documented by Luo et al. (2022). The seasonal patterns reflect the close linkage between NH_3 distribution and region-specific anthropogenic activities, alongside seasonal natural processes. These spatial patterns exhibit general consistency with results from IASI (e.g., Van Damme et al., 2015) and CrIS (e.g., Shephard et al., 2020).

We note that these weekly global maps may still be influenced by short-term episodic events, such as biomass burning. Therefore, they are used here primarily as representative examples of the constellation-derived global NH_3 spatial distributions. The more quantitative regional diurnal and seasonal analyses in Section 3.2 are based on full-month averages using all available observations in each selected month.

(a) January 12-18, 2024

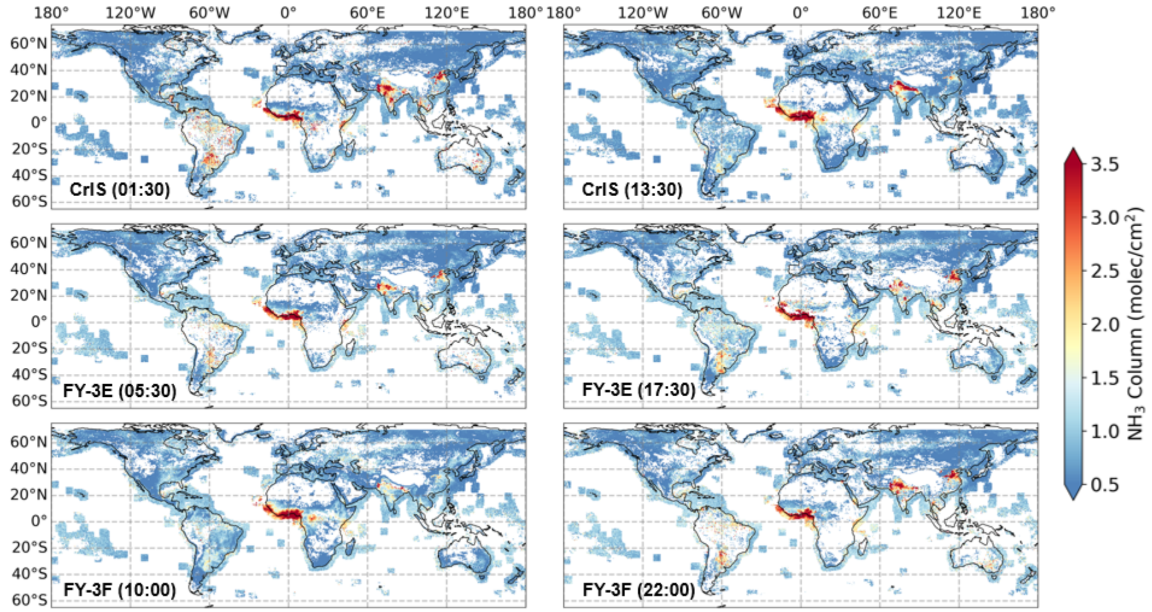

(b) April 12-18, 2024

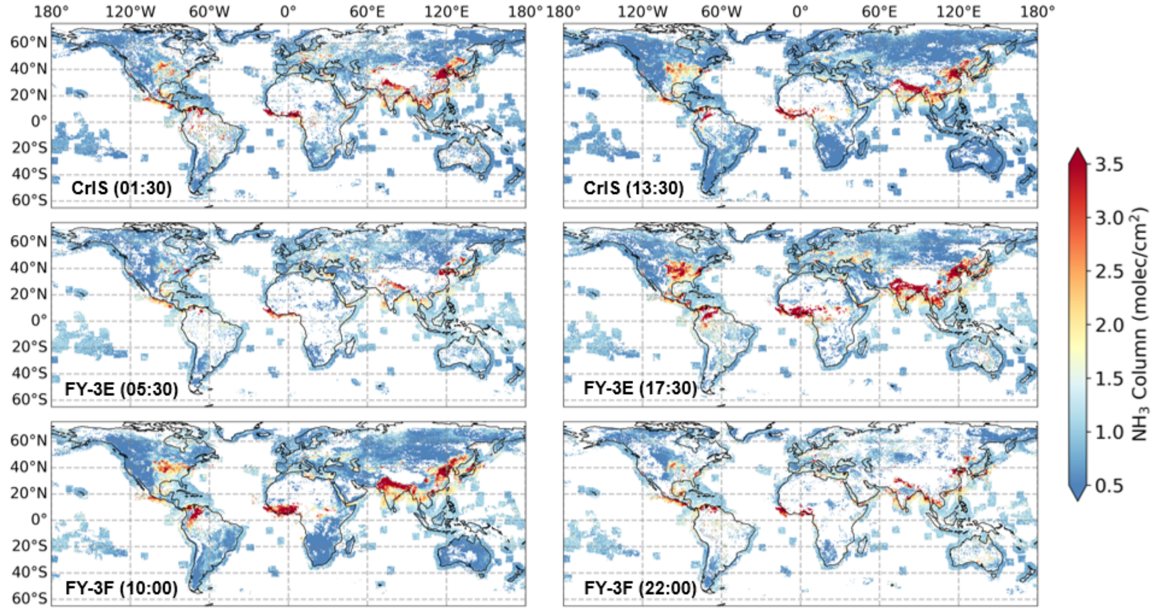

Figure 2. Representative seven-day mean NH_3 columns retrieved from FY-3E, FY-3F, and CrIS for six different time slots, gridded to a 0.5° × 0.5° spatial resolution. The data correspond to the period of (a) January 12–18, 2024 and (b) April 12–18, 2024.

(a) July 17-23, 2024

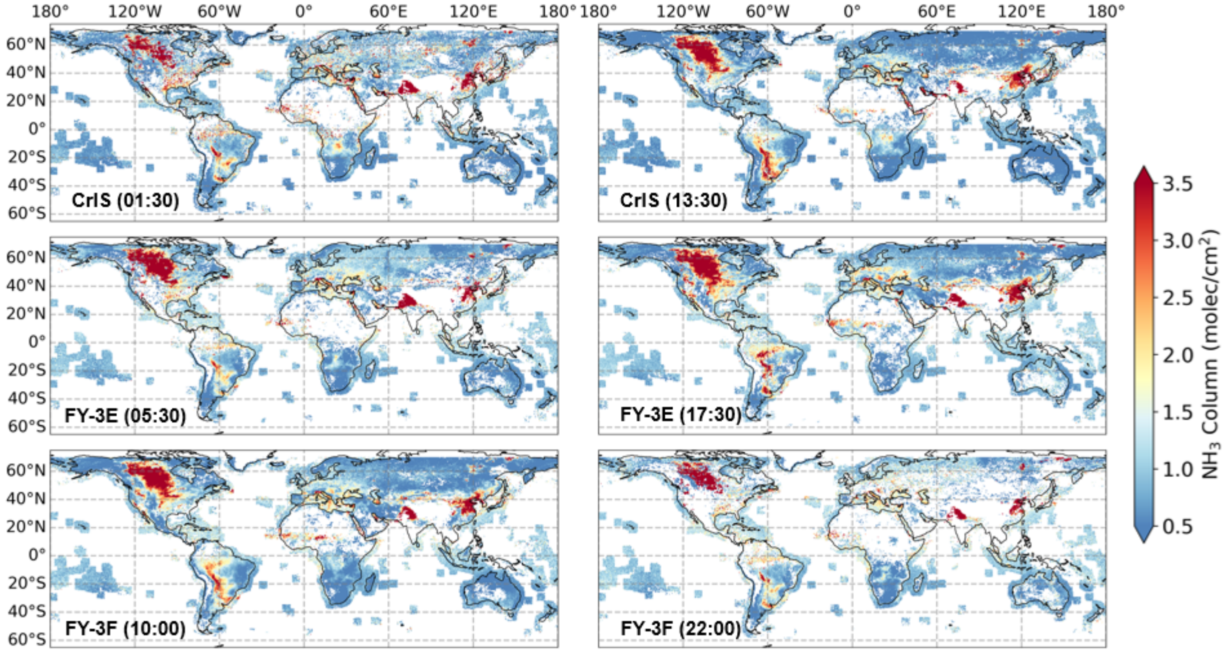

(b) October 1-7, 2024

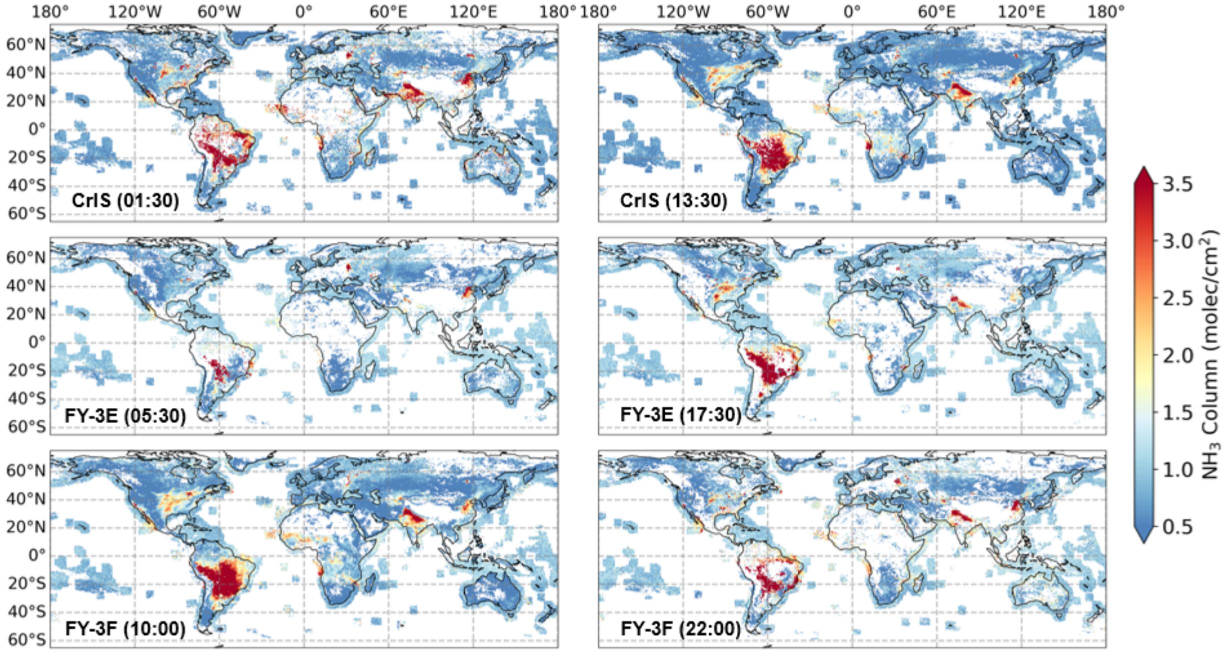

Figure 3. Same as Fig. 2, but for the period of (a) July 17–23, 2024 and (b) October 1-7, 2024.

3.2 NH_3 variations in global major source regions from the LEO constellation

To conduct in-depth analysis of NH_3 variations, we select three major emission hotspots, locating inside the North China Plain (118°E, 37°N), the Indo-Gangetic Plain (78°E, 28°N), and Central United States (100.5°W, 36.5°N), respectively. These hotspots are characterized by intensive agricultural activities and high livestock densities, consistent with the high-emission areas for their substantial NH_3 column abundances and distinct diurnal and seasonal dynamics. For each hotspot, we extract data within a 2.5° × 2.5° grid centered at the specified coordinates, covering six overpass times per day. A 2.5° × 2.5° box is selected to balance spatial representativeness and sample size. Because the analysis separates retrievals by satellite overpass time and month and further applies strict quality filters, a smaller box would often lead to insufficient valid retrievals, especially during nighttime or low-sensitivity conditions. The selected box size provides enough samples for stable monthly means while still focusing on the core NH_3 hotspot regions. The monthly mean is calculated only when the number of filtered retrievals within the 2.5° × 2.5° box exceed 10 during that month. TC affects the retrieval accuracy (Bauduin et al., 2017) and that higher absolute TC contributes to better retrievals (Clarisse et al., 2010). When TC is close to zero, the NH_3 spectral signal becomes weak and the retrieval sensitivity decreases, whereas a larger absolute TC generally enhances the spectral signal and improves the retrieval sensitivity. To ensure high quality NH_3 columns retrievals, we apply stricter sensitivity filters than those used for the global spatial-distribution maps in Section 3.1. Specifically, the same basic quality-control criteria are used, but the TC and AVK thresholds are tightened from absolute TC > 3 K and surface layer AVK value > 0.1 to absolute TC > 5 K and surface layer AVK value > 0.3. These stricter criteria are adopted to reduce the influence of local-time-dependent retrieval sensitivity on the inferred diurnal cycles, because TC itself has a pronounced diurnal variation.

The diurnal cycles of full-month averaged NH_3 columns for the three hotspots in each selected month are presented in Fig. 4, with IASI NH_3 ANNI V4.0 product overlaid for comparison. Also shown are the monthly mean planetary boundary layer heights (BLH) from ERA5 reanalysis. All three hotspots exhibit consistent seasonal differences in diurnal variability, a pattern that is consistent with the findings of Clarisse et al. (2021) from GIIRS observations and aligns with broader research on NH_3 dynamics (Tevlin et al., 2017). Warmer months (April–September) show distinct day-night contrasts, while winter months (December–February) display minimal diurnal fluctuations.

For the North China Plain (Fig. 4a), FY-3E, FY-3F, CrIS, and IASI data collectively reveal that warm-season NH_3 columns follow a clear diurnal pattern with a peak between 10:00 and 13:30 local solar time (LST), and nighttime values approximately 50–60% lower than daytime maxima. The peak corresponds to intensified agricultural activities (e.g., fertilization and livestock management) and temperature-driven volatilization from soils and animal waste, mechanisms identified by Ernst and Massey (1960) and Sutton et al. (2013) as primary drivers of daytime NH_3 emission enhancement. Higher BLH during the day facilitates vertical diffusion of NH_3 and contributes to the observed column dynamics (Saylor et al., 2010). In contrast, winter NH_3 columns over the North China Plain show negligible diurnal variation, which is probably due to the fact that cold-season emissions are limited by low temperatures and reduced agricultural activity (Kuang et al., 2020; Clarisse et al., 2021).

The Indo-Gangetic Plain (Fig. 4b) exhibits the highest overall NH_3 columns among the three hotspots, with warm-season daytime columns nearly double those of the North China Plain. This regional difference stems from higher concentrations of NO_x and SO_2 (Clarisse et al., 2021; Ding et al., 2024) over the North China Plain that act as neutralizing agents, shortening the lifetime of atmospheric NH_3 (Liu et al., 2018; Wang et al., 2020). The most pronounced warm-season diurnal amplitude appears in the Indo-Gangetic Plain, with daytime columns up to three times higher than nighttime values. This pattern reflects the region's intensive irrigated agriculture, high livestock density (Perrone, 2020), and the exponential dependence of NH_3 emissions on temperature (Hempel et al., 2016). Winter diurnal variations here are similarly weak, though NH_3 columns remain higher than those in the other two regions due to persistent agricultural activity in milder winter conditions (Saraswati et al., 2018).

For the Central U.S. (Fig. 4c), the diurnal variation pattern is broadly consistent with the Asian regions but with a smaller amplitude. Warm-season NH_3 columns peak between 11:00 and 14:00 LST, with daytime values approximately 1.5–2 times higher than nighttime levels, while winter columns show little diurnal fluctuation. This consistency supports that temperature, BLH dynamics, and diurnal emission sources (e.g., agricultural activities) are universal drivers of NH_3 diurnal cycles across high-emission regions globally, which is evidenced by Saylor et al. (2010) from their analysis of NH_3 measurements in the southeastern U.S.. The smaller amplitude compared to the Indo-Gangetic Plain likely reflects moderate temperature variations and balanced NH_3 emission and deposition processes, as reported by Warner et al. (2017) in satellite observations of North American agricultural regions. Li et al. (2025) further emphasize that local deposition in vegetation-dense areas offsets large-scale transport, explaining the muted diurnal amplitude relative to Asian regions.

The spatial and seasonal dynamics of NH_3 columns are further illustrated in Figs. 5–7 for the North China Plain, Indo-Gangetic Plain, Central U.S., respectively, retrieved by FY-3E/HIRAS-II, FY-3F/HIRAS-II and CrIS. Fig. A1 further illustrates monthly mean NH_3 columns variations for these three regions, confirming consistent time series across the six daily satellite overpasses and coherent seasonal trends. All three regions exhibit a consistent seasonal peak in NH_3 columns during spring to summer (March–August), with the lowest values in winter (December–February). For the North China Plain, all retrievals at six distinct times show that NH_3 columns peak in June, with spatial coverage expanding across the entire plain during warm months, reflecting widespread agricultural activities (e.g., wheat fertilization and livestock waste management) and favorable meteorological conditions for emission (Zhang et al., 2010; Zhan et al., 2021). In contrast, winter maps display sparse, localized high-NH_3 patches, consistent with reduced agricultural activity and lower temperature-driven volatilization (Schjoerring et al., 1998).

For the Indo-Gangetic Plain, Fig. 6 shows that the region maintains the highest NH_3 columns year-round, with spatial hotspots concentrated in the central plain during both day and night. However, daytime maps exhibit broader coverage extending to the plain's peripheries, while nighttime maps show more concentrated hotspots near emission sources. For the central U.S., Fig. 7 reveals the lowest overall NH_3 columns among the three regions, with daytime spatial patterns spreading across the Corn Belt and Great Plains, and nighttime patterns contracting to smaller agricultural clusters.

The comparison between daytime and nighttime spatial patterns underscores the critical role of BLH in shaping NH_3 distribution. Daytime maps display broader spatial coverage because higher BLH (typically 1–3 km during warm-season days) facilitates vertical and horizontal diffusion of NH_3 away from emission sources. In contrast, nighttime maps show more localized NH_3 columns, as lower BLH (often <500 m at night) traps emissions near the surface (Walker et al., 2006; Wang et al., 2019). This pattern is especially pronounced over the North China Plain, where Figs. 5b-5d show contiguous high-NH_3 zones across the plain, while Fig. 5a, 5e and 5f limit high columns to central agricultural districts. For the Indo-Gangetic Plain, nighttime spatial maps also reveal persistent NH_3 in the residual layer, an effect linked to BLH collapse in the evening, which traps NH_3 at higher altitudes for several hours (Lonsdale et al., 2017; Kuang et al., 2020). This residual layer NH_3 explains why some nighttime retrievals show broader coverage than expected, even with low BLH, and aligns with Clarisse et al. (2021)'s observation that NH_3 vertical profile assumptions can impact nighttime retrieval accuracy.

To assess the impact of the filters on the retrieved NH_3 diurnal variation, we perform an additional sensitivity analysis using three filtering configurations. A loose filter with surface AVK > 0.1 and absolute TC > 3 K, the current hotspot filter with surface layer AVK value > 0.3 and absolute TC > 5 K, and a stricter filter with surface layer AVK value > 0.4 and absolute TC > 7 K. The remaining quality-control criteria are kept consistent among the three configurations. The resulting spatial distributions over the North China Plain and Indo-Gangetic Plain and the corresponding diurnal cycles are shown in the Supplementary Figs. S7–S10. The total numbers of quality-controlled retrievals retained for each satellite under the different filtering configurations are also reported in the subpanels. The three filtering configurations lead to different data-retention rates, as expected, but the major NH_3 hotspot patterns remain spatially similar and the regional diurnal cycles are not substantially distorted. This indicates that the main diurnal features discussed here are not strongly affected by the selected absolute TC and surface AVK thresholds, although the absolute column values and sampling density remain sensitive to filtering strength.

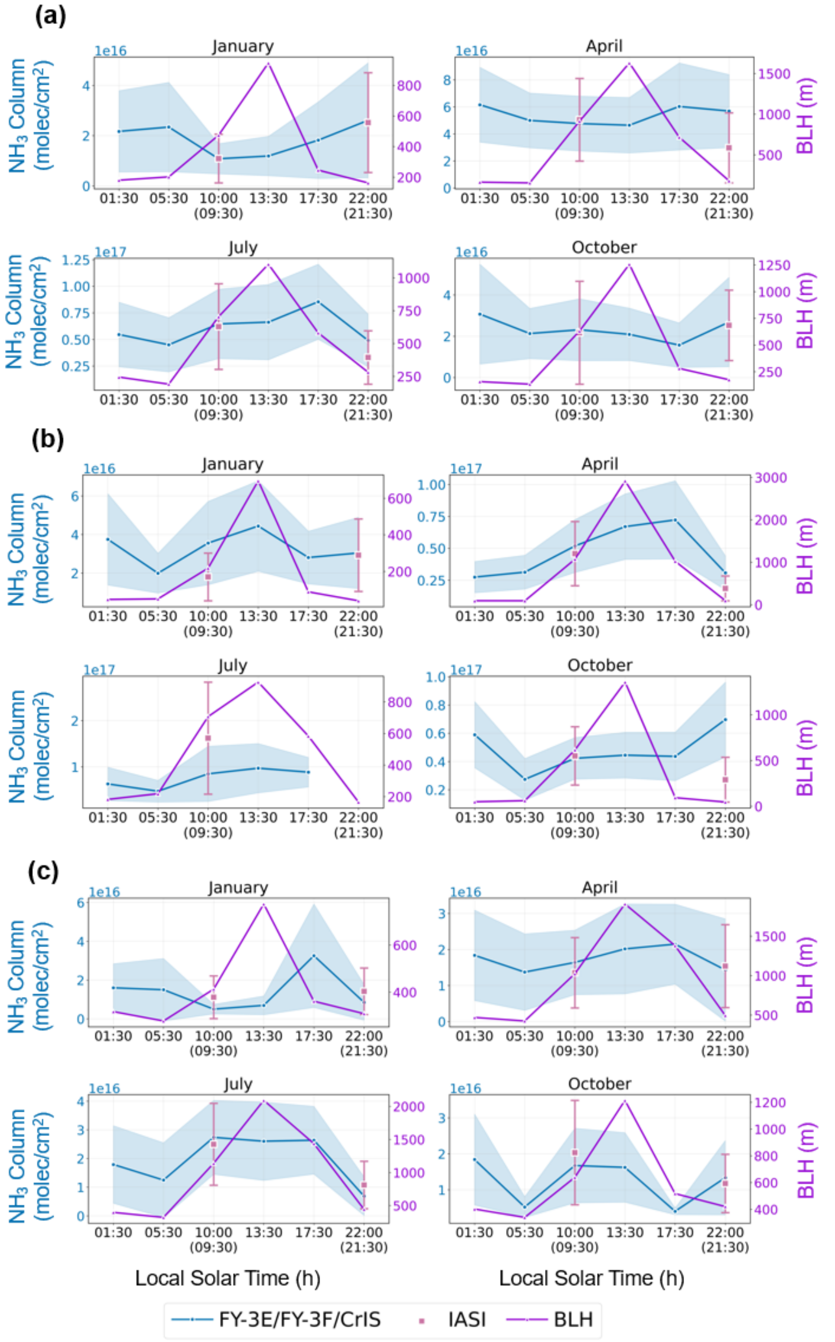

Figure 4. Diurnal cycles of retrieved NH$_3$ columns from FY-3E, FY-3F and CrIS over (a) the North China Plain (118°E, 37°N), (b) the Indo-Gangetic Plain (78°E, 28°N), and (c) Central U.S. (100.5°W, 36.5°N). The locations of these three sites are indicated in Figs. 5-7, respectively. Blue circles denote the mean values within the 2.5° × 2.5° grid, and the blue shaded area represents the standard deviation for each overpassing time. IASI retrieval results for the same region are overlaid for comparison: reddish purple squares indicate IASI mean values, with error bars representing their standard deviation. The time axis is expressed in Local Solar Time. The diurnal variation of monthly mean planetary boundary layer height (BLH) is also plotted in purple.

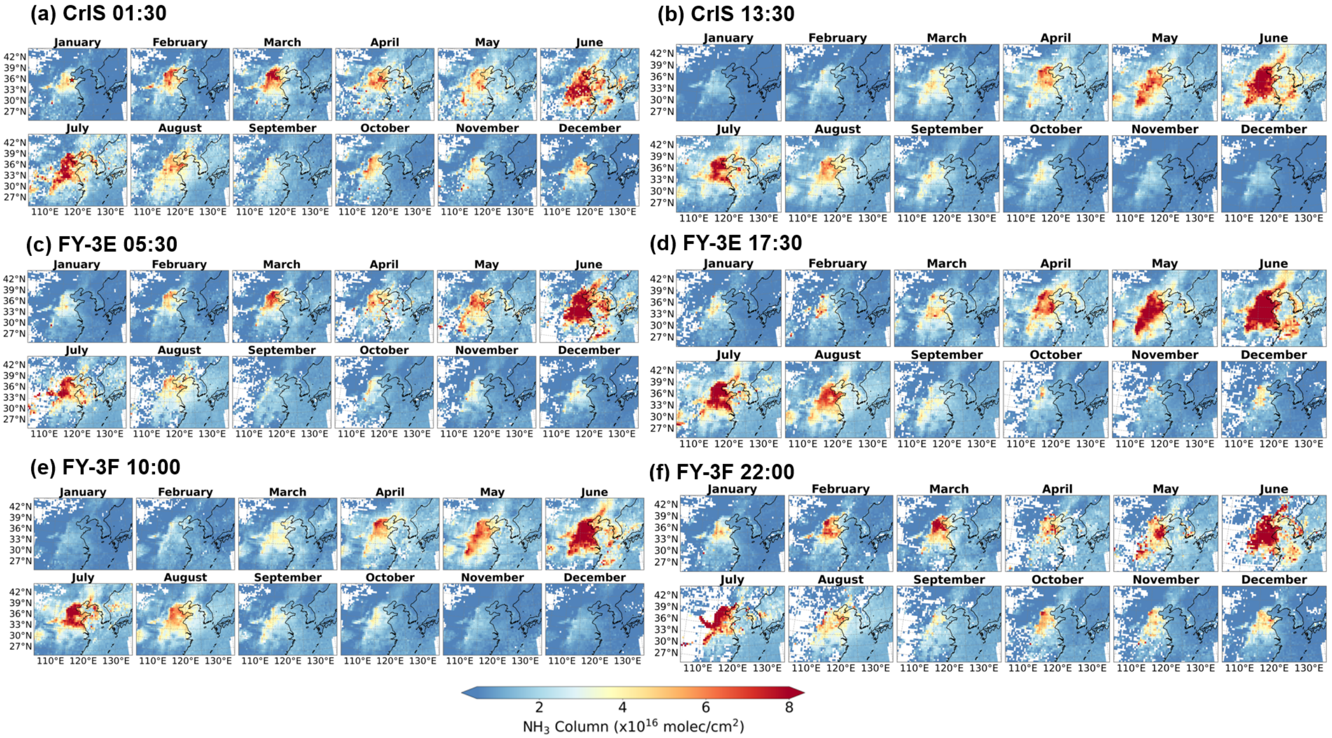

Figure 5. Monthly mean NH$_3$ columns (0.5° × 0.5° grid) over the North China Plain retrieved by (a) CrIS at night overpasses (01:30 LST), (b) CrIS at daytime overpasses (13:30 LST), (c) FY-3E/HIRAS-II at dawn overpasses (05:30 LST), (d) FY-3E/HIRAS-II at dusk overpasses (17:30 LST), (e) FY-3F/HIRAS-II at morning overpasses (10:00 LST), and (f) FY-3F/HIRAS-II at night overpasses (22:00 LST), during 2024. The red star in the January panel of Fig. 5a indicates the location of the site (118°E, 37°N) analyzed in Figs. 4 and 8.

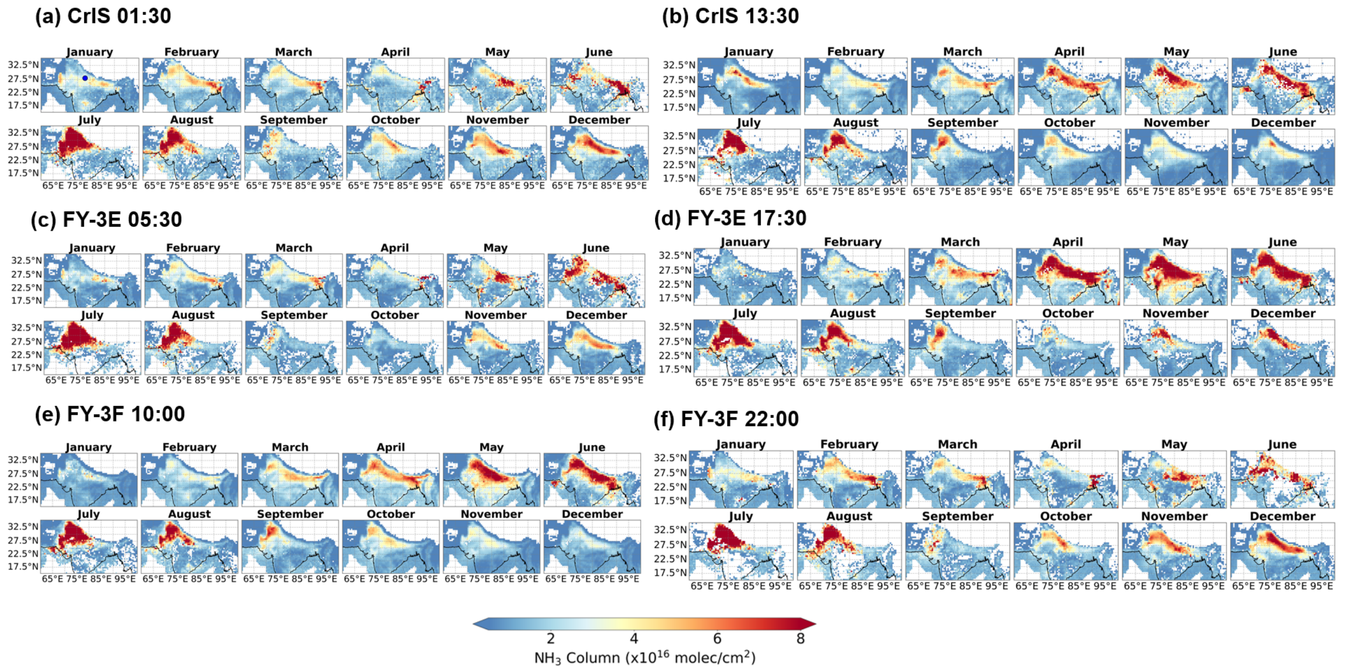

Figure 6. Same as Fig. 5, but for the Indo-Gangetic Plain. The blue circle in the January panel of Fig. 6a indicates the location of the site (78°E, 38°N) analyzed in Figs. 4 and 8.

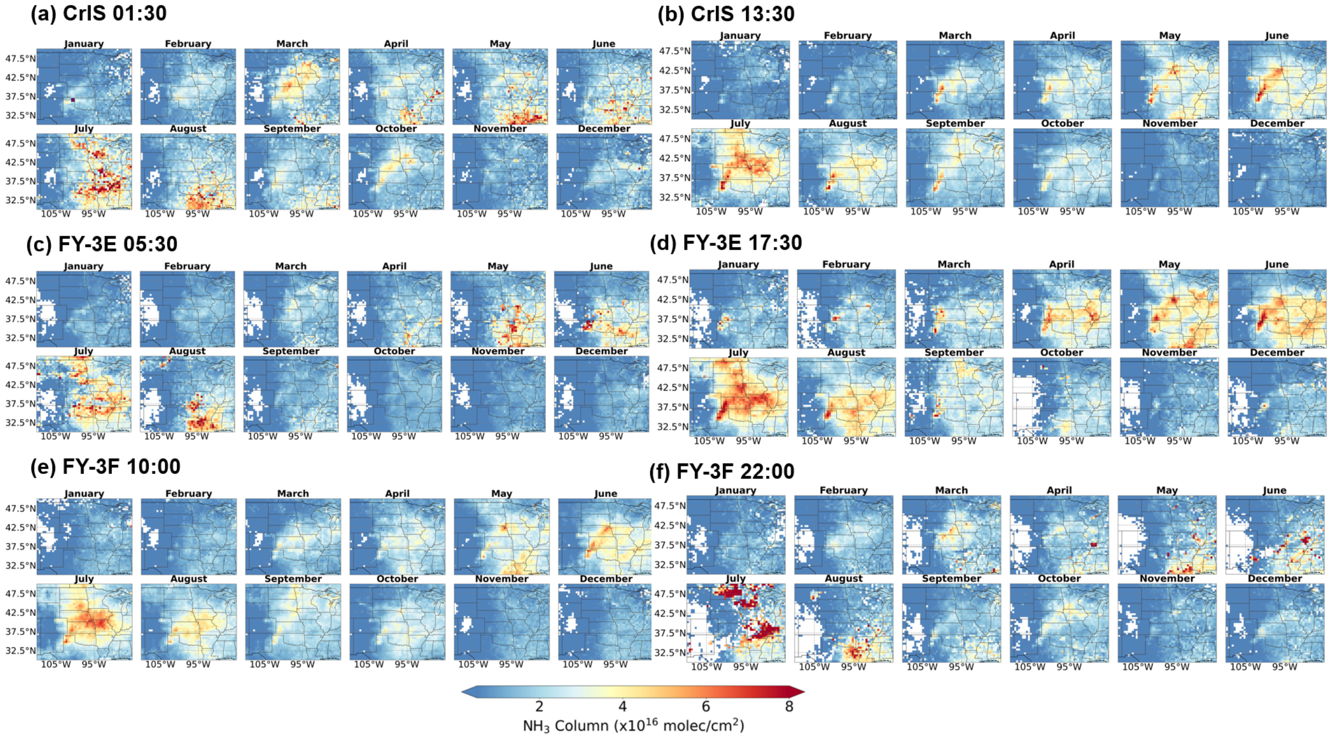

Figure 7. Same as Fig. 5, but for Central U.S.. The purple square in the January panel of Fig. 7a indicates the location of the site (100.5°W, 36.5°N) analyzed in Figs. 4 and 8.

3.3 Cross-comparison with geostationary FY-4B/GIIRS and ground-based FTIR NH_3 observations

To evaluate the consistency of NH_3 column retrievals from the polar-orbiting constellation, we perform spatiotemporally collocated cross-comparisons between FY-3E/HIRAS-II, FY-3F/HIRAS-II, CrIS, and geostationary FY-4B/GIIRS retrievals. The comparisons are conducted over the Indo-Gangetic Plain (75°E–95°E, 15°N–35°N) and the North China Plain (110°E–130°E, 25°N–45°N), where strong NH_3 signals are frequently observed and FY-4B/GIIRS provides geostationary coverage. A polar-orbiting retrieval and a FY-4B/GIIRS retrieval are considered collocated when their longitude and latitude differences are both less than 0.5° and their observation time difference is less than 0.5 h. These thresholds are selected as a compromise between retaining sufficient matched samples and minimizing spatial and temporal representativeness differences.

The comparisons in Fig. 8 also show broad consistency across the matched local overpass periods sampled by the three polar-orbiting sensors. Here, the observational periods refer to the local-time periods of the polar-orbiting observations collocated with FY-4B/GIIRS, namely CrIS at 01:30/13:30, FY-3E/HIRAS-II at 05:30/17:30, and FY-3F/HIRAS-II at 10:00/22:00. The agreement across these matched local-time periods indicates that the constellation retrievals are generally consistent with FY-4B/GIIRS over both nighttime/dawn and daytime/dusk observations, although the agreement is typically stronger during daytime because of larger thermal contrast and higher retrieval sensitivity.

We further perform seasonal comparisons between each polar-orbiting sensor and FY-4B/GIIRS using the same collocation and quality-filtering criteria. These results are shown in the Figs. A2. The seasonal regression slopes mostly fall within the range of 0.7–1.1. The slopes slightly below unity in the annual comparison should not be interpreted as clear evidence of a persistent systematic bias in either FY-4B/GIIRS or the polar-orbiting retrievals. Instead, the remaining differences likely due to their differences in retrieval sensitivity, collocation representativeness, sampling footprints, viewing geometry, and vertical sensitivity. These factors are particularly important for NH_3 because of its short atmospheric lifetime and strong spatial heterogeneity.

We also compare the polar-orbiting satellite retrievals with ground-based FTIR NH_3 column measurements at Hefei, China (Wang et al., 2022). Satellite retrievals within a 1° × 1° spatial window and a 1 h temporal window around the FTIR observations are averaged and compared with the corresponding measurements. The comparison is shown in Fig. A3. The satellite retrievals show reasonable consistency with the FTIR observations, although the collocated numbers are limited, with slopes of 0.87 ± 0.22, 1.03 ± 0.08, and 1.13 ± 0.18 for FY-3E/HIRAS-II, FY-3F/HIRAS-II, and CrIS, respectively. The corresponding RMSE values range from 7.80×10^{15} to 1.11×10^{16} molec/cm^2. Overall, the annual and seasonal FY-4B/GIIRS comparisons, together with the Hefei FTIR comparison, support the broad consistency of the LEO constellation retrievals in capturing major NH_3 spatial and temporal variability.

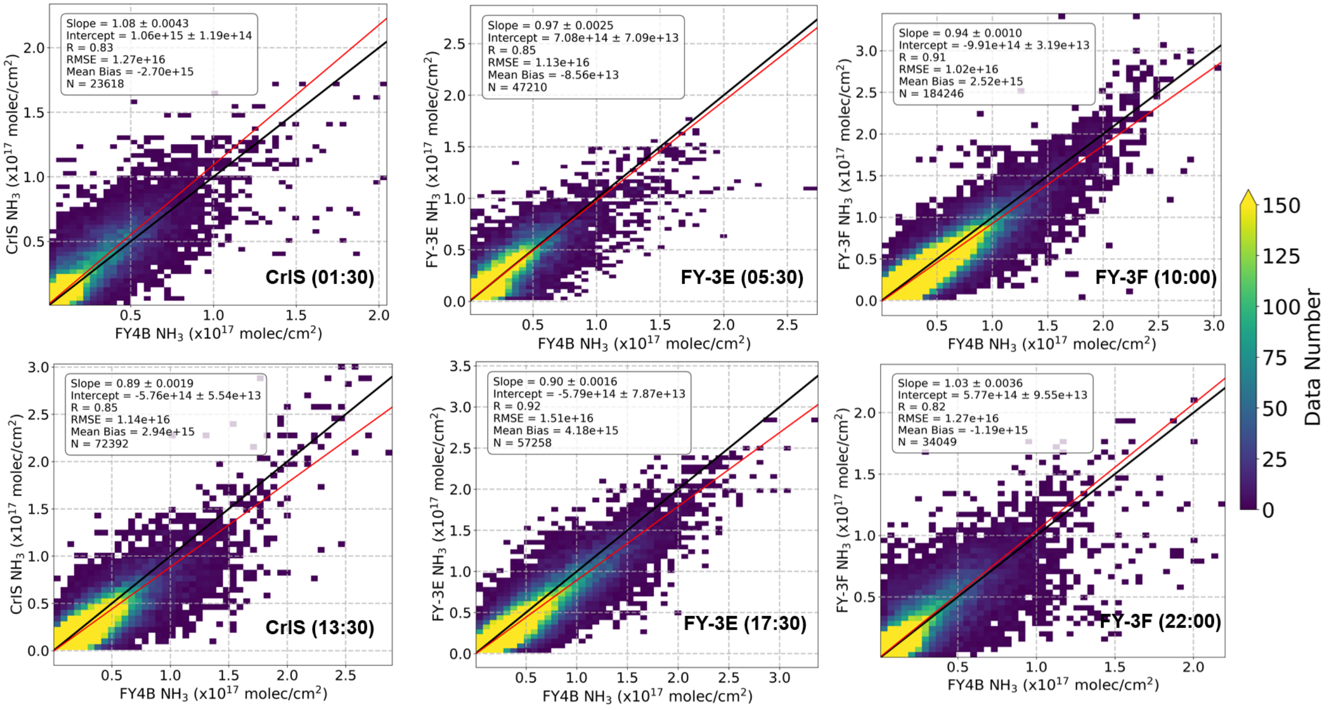

Figure 8. Comparisons of NH3 columns between polar-orbiting satellites (FY-3E/HIRAS-II, FY-3F/HIRAS-II and CrIS) retrievals and geostationary satellite (FY-4B/GIIRS) retrievals over the Indo-Gangetic Plain (75°E-95°E, 15°N-35°N) and the North China Plain (110°E-130°E, 25°N-45°N) at different times of the day in 2024. Observations are collocated when the differences in longitude and latitude are both less than 0.5° and observation time is less than 0.5 hours. The black dashed line represents the 1:1 equivalence line, with the red line indicating the orthogonal distance regression (ODR) fit. The fit's slope, intercept, correlation coefficient (R), and root mean square error (RMSE), mean bias (calculated as polar satellite retrievals minus geostationary satellite retrievals), data number are also provided.

3.4 Diurnal variations of the surface AVK, the retrieval uncertainty and the TC

Fig. 9 presents the diurnal and seasonal dynamics of surface AVK, TC, and column retrieval uncertainty over three representative hotspots, locating in the North China Plain (118°E, 37°N), the Indo-Gangetic Plain (78°E, 28°N), and the Central U.S. (100.5°W, 36.5°N). The statistics are derived from FY-3E/HIRAS-II, FY-3F/HIRAS-II, and CrIS retrievals within 2.5° × 2.5° boxes and are shown as monthly averages for January, April, July, and October across six local overpass times. To clarify the robustness of these monthly averages, the number of valid retrievals used for each region, month, and overpass time is provided in Table S2. Monthly means are shown only when more than 10 quality-controlled retrievals are available.

TC exhibits a consistent diurnal pattern across all regions. Midday overpasses (10:00–13:30 local solar time) see TC peak with positive values ranging from 5 to 12 K in warm months (April and July), while nighttime and early morning (01:30–05:30) bring near-zero or negative TC, particularly in January and October. Seasonal contrasts in TC amplitude are striking.

Warm months feature fluctuations of up to 15 K in the Indo-Gangetic Plain, driven by intense solar heating, while cold months (January) show smaller variations, with TC confined to ±5 K for most overpasses.

The surface layer value of column AVK, which quantifies the observational information content related to near-surface NH_3, tracks TC closely across all regions and seasons. Midday overpasses coincide with peak surface layer column AVK (0.3–0.6), indicating robust sensitivity to near-surface NH_3 variations when TC is strongest. In contrast, surface layer column AVK at nighttime and dawn drops to 0.1–0.3, especially in January. The Indo-Gangetic Plain exhibits the most pronounced diurnal swings, with July midday surface layer column AVK exceeding 0.6, while the Central U.S. maintains more moderate, stable values (0.2–0.4) across all seasons. Seasonally, surface layer column AVK remains consistently higher in April and July relative to January and October, confirming that warm-season midday conditions offer the most useful observational constraints for NH_3 retrievals.

Column retrieval uncertainty generally decreases under conditions with larger absolute TC and higher surface AVK, but this relationship is not purely inverse and should not be interpreted as strictly monotonic. In particular, strongly negative TC can also enhance thermal infrared sensitivity because absorption-like spectral features may become emission-like features, as shown for lower-tropospheric pollution retrievals by Boynard et al. (2014). Therefore, TC should be interpreted together with AVK and retrieval uncertainty, rather than as a standalone monotonic sensitivity indicator.

Daytime bins often contain more valid retrievals than nighttime or dusk/evening bins, but the pattern is not uniform across regions and months (Table S2). Some bins have relatively sparse sampling, such as the Indo-Gangetic Plain in July at 05:30 and 22:00 and Central U.S. in October at 17:30, whereas other daytime bins contain more than 1000 valid retrievals. These differences mainly reflect the combined effects of cloud screening and sensitivity-related quality filters.

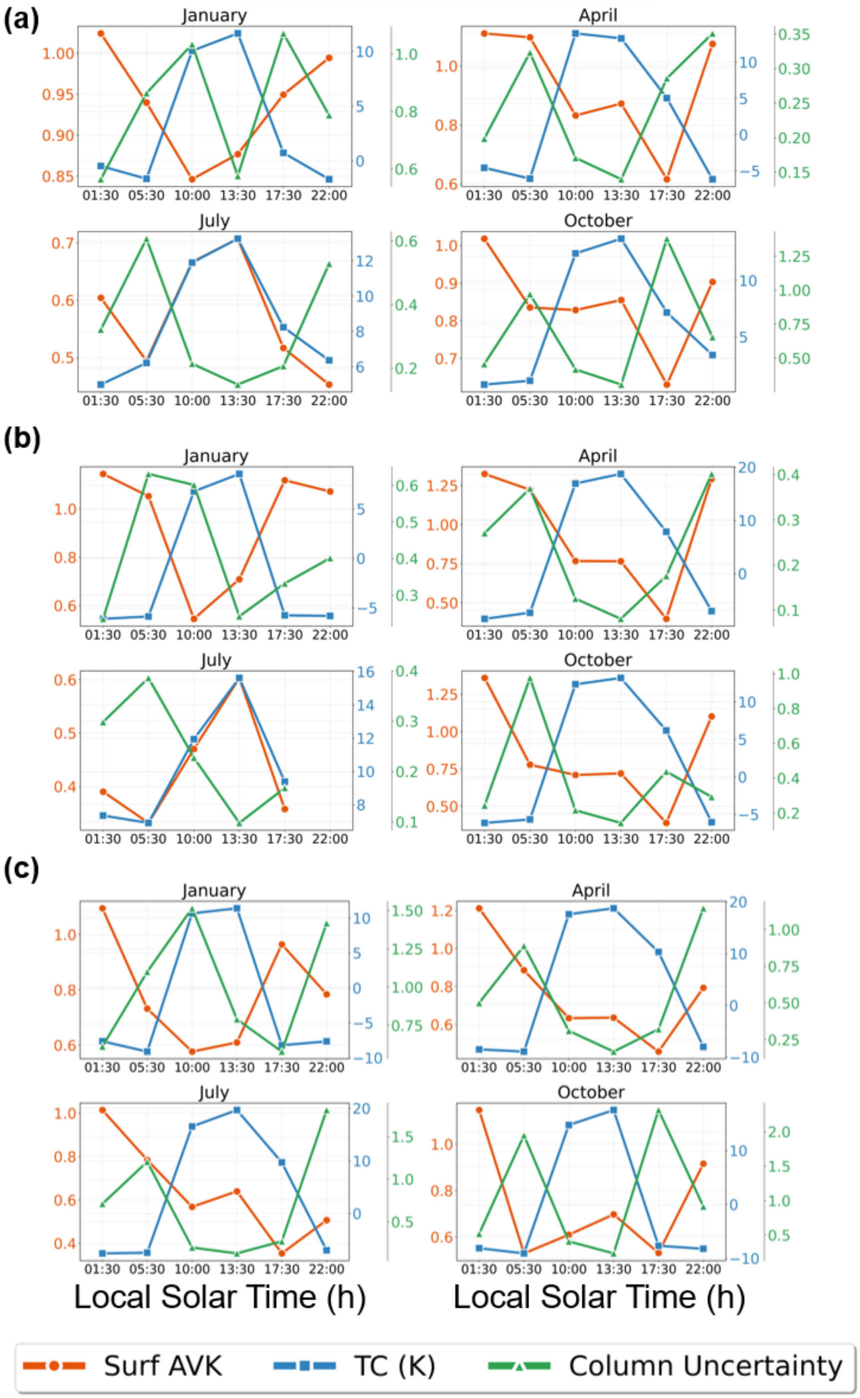

Figure 9. Diurnal cycle of surface AVK, TC and column uncertainty from FY-3E, FY-3F and CrIS over three hotspots in (a) the North China Plain (118°E, 37°N), (b) the Indo-Gangetic Plain (78°E, 28°N), and (c) Central U.S. (100.5°W, 36.5°N). The number of valid retrievals used for each monthly mean is provided in Table S2.

4 Conclusions

This study develops a global monitoring framework by integrating three polar-orbiting hyperspectral infrared sounders, including FY-3E/HIRAS-II in a dawn-dusk orbit, FY-3F/HIRAS-II in a mid-morning orbit, and CrIS in an afternoon orbit. This constellation achieves quasi-geostationary-like coverage, enabling six global NH_3 column retrievals based on the optimal estimation method, for every 4-hour per day. This framework successfully captures spatial, diurnal, and seasonal dynamics of tropospheric NH_3 worldwide, with elevated columns consistently identified in major agricultural hotspots. Annual and seasonal cross-comparisons with geostationary FY-4B/GIIRS show broad consistency between the LEO constellation retrievals and GIIRS over the matched local overpass periods, including CrIS at 01:30/13:30, FY-3E/HIRAS-II at 05:30/17:30, and FY-3F/HIRAS-II at 10:00/22:00. An additional comparison with ground-based FTIR observations at Hefei provides independent support for the reliability and consistency of the retrievals.

Key findings indicate that temperature-dependent volatilization, boundary-layer dynamics, and agricultural activity patterns jointly regulate the diurnal and seasonal variability of NH_3. Differences among regions are further modulated by source strength, fertilizer and livestock management practices, meteorological conditions, and atmospheric chemical processing. The constellation effectively addresses the longstanding gap of high-frequency NH_3 observations in regions lacking geostationary satellite coverage, providing a comprehensive dataset for global NH_3 cycling research.

Looking forward, the upcoming integration of FY-3H/HIRAS-II launched at the end of 2025, equipped with the same HIRAS-II sensor as FY-3E and FY-3F, will homogenize the constellation, further enhancing data consistency and spatial-temporal coverage. This refined system holds great potential to advance NH_3 emission quantification, improve parameterizations in global climate and air quality models, and support evidence-based policies for anthropogenic source management. Future work could focus on optimizing NH_3 vertical profile parametrization, cross-calibrating between sensors onboard different satellite for enhanced retrieval accuracy and consistency, and expanding the constellation's applications to study NH_3's links with aerosol formation, acid deposition, and ecosystem impacts. To summarize, this framework demonstrates the value of synergizing polar-orbiting satellites to strengthen global atmospheric composition monitoring, contributing to more effective mitigation of NH_3-related environmental and climate effects.

Appendix A

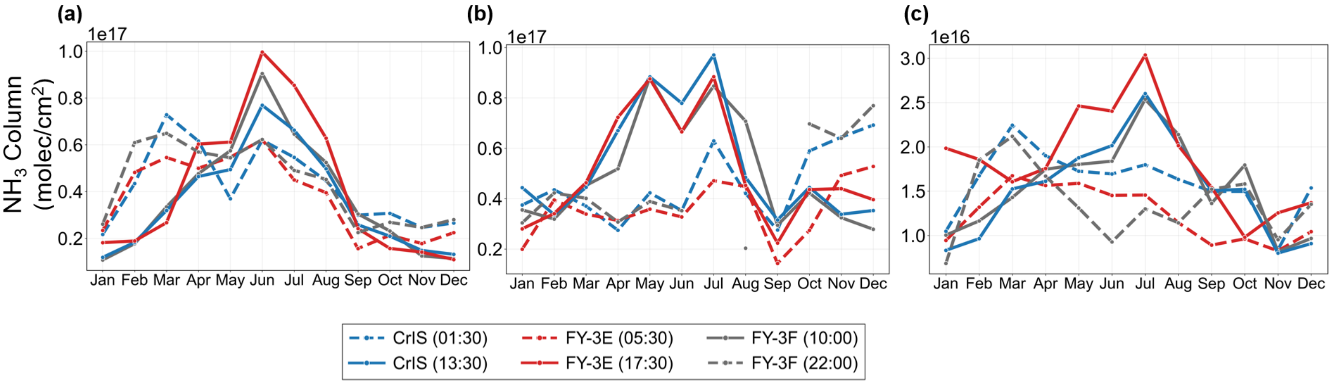

Figure A1. Seasonal variation timeseries of retrieved NH₃ columns over (a) the North China Plain, (b) the Indo-Gangetic Plain and Central U.S.

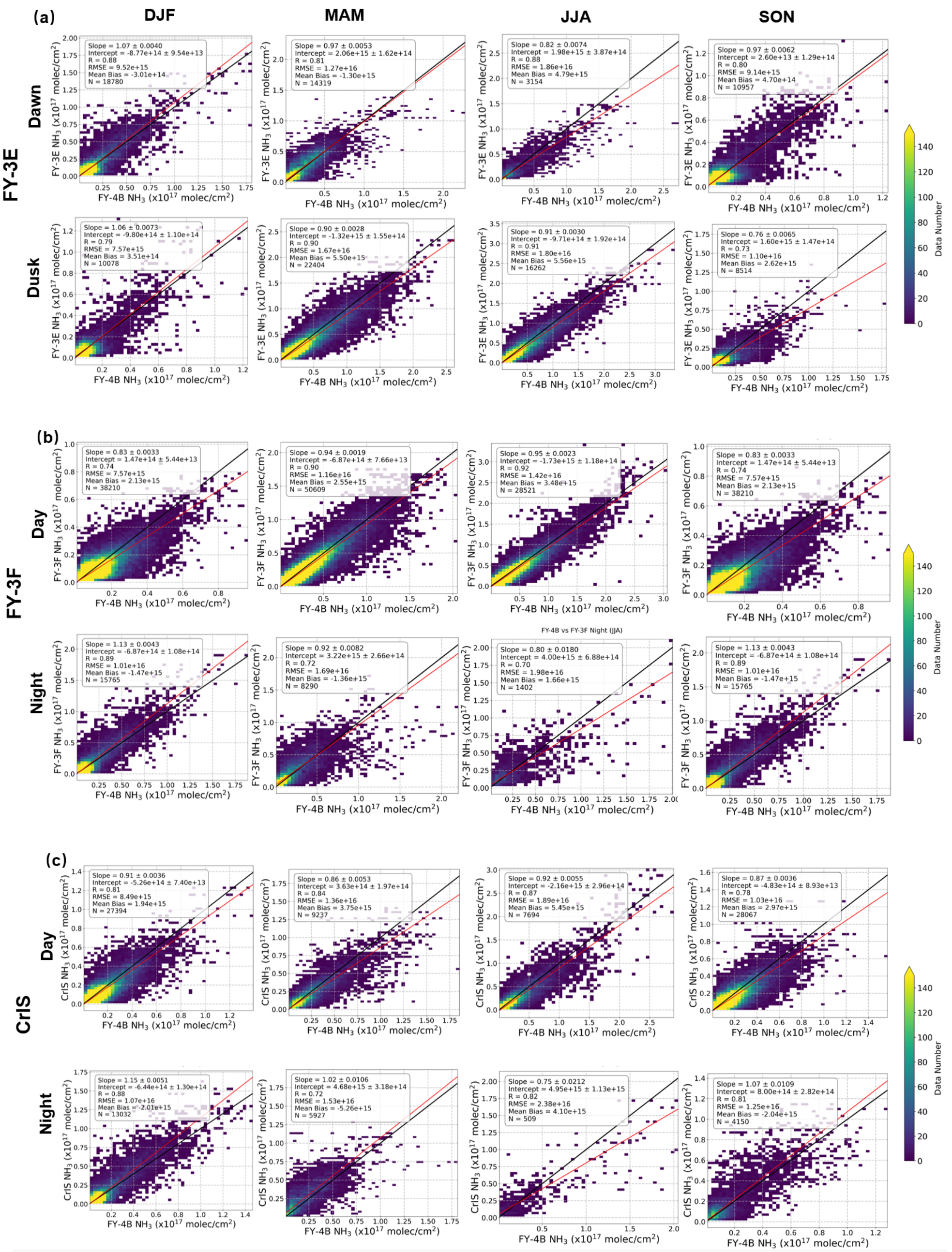

Figure A2. Same as Fig. 8, but for seasonal comparisons between FY-3E/HIRAS-II (a), FY-3F/HIRA-II (b), CrIS (c) and FY-4B/GIIRS over the Indo-Gangetic Plain and the North China Plain. DJF, MAM, JJA, and SON denote December–January–February, March–April–May, June–July–August, and September–October–November, respectively. The black solid line represents the 1:1 line, and the red solid line indicates the orthogonal distance regression (ODR) fit. The slope, intercept, correlation coefficient (R), root mean square error (RMSE), mean bias, and number of collocated samples are provided in each panel.

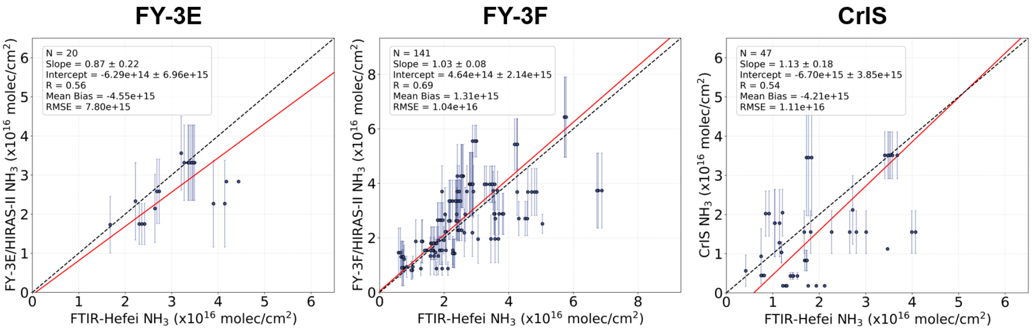

Figure A3. Validations with ground-based FTIR in Hefei, China. The black dashed line represents the 1:1 equivalence line, with the red line indicating the orthogonal distance regression (ODR) fit. The fit's slope, intercept, correlation coefficient (R), root mean square error (RMSE), mean bias (calcucated as polar satellite retrievals minus ground-base measurement), and data number are also provided. The dot represents the mean value of satellite retrieved NH_3 columns and the error bar represents 1 standard deviation. If there is only one match point, the error bars are not displayed.

Data availability

The FY-3E and FY-3F NH_3 retrieval datasets are publicly available at ZENODO (https://doi.org/10.5281/zenodo.18359451 and https://doi.org/10.5281/zenodo.18366114, respectively). Currently, the FY-3E dataset is available from January 2023 to December 2024, and the FY-3F dataset is available from January to December 2024. The GIIRS NH_3 data (from July 2022 to June 2025) used in this study are publicly available on Zenodo (https://doi.org/10.5281/zenodo.17193848). Further updates on FengYun NH_3 data will be provided on the project website (https://fengyunair.github.io/). FengYun satellite Level 1 data are publicly available from the FengYun Satellite Data Center at http://satellite.nsmc.org.cn/portalsite/default.aspx. The IASI NH_3 ANNI V4.0 product is available from the AERIS data infrastructure (https://iasi.aeris-data.fr/). The CrIS L1 spectra are publicly available from https://search.earthdata.nasa.gov/.

Author contributions

ZZ designed the experiments, and JH carried them out. ZZ and JH developed the model code and JH performed the simulations. MS and RZ assisted the satellite data pre-processing and results analysis. JH prepared the manuscript with contributions from all co-authors.

Competing interests

At least one of the (co-)authors is a member of the editorial board of Atmospheric Measurement Techniques.

Acknowledgements

We gratefully acknowledge Drs. Chengli Qi, Lu Lee, Xiuqing Hu, and Feng Lu from the National Meteorological Satellite Center of China for their guidance on using the FengYun hyperspectral infrared spectra observations. We would also like to thank Drs. Cathy Clerbaux, Lieven Clarisse and Martin Van Damme for making the IASI NH_3 data publicly available. We thank Dr. Wei Wang from the Chinese Academy of Sciences for providing the Heifei-FTIR NH_3 data.

Financial support

Z.-C. Zeng acknowledges funding from the National Natural Science Foundation of China (grant nos. 42275142), the National Key R&D Program of China (grant no. 2026YFE0102400). This work was also supported by High-performance Computing Platform of Peking University.

References

Abbatt, J. P. D., Benz, S., Cziczo, D. J., Kanji, Z., Lohmann, U., and Möhler, O.: Solid Ammonium Sulfate Aerosols as Ice Nuclei: A Pathway for Cirrus Cloud Formation, Science, 313, 1770–1773, https://doi.org/10.1126/science.1129726, 2006.

Adams, P. J., Seinfeld, J. H., Koch, D., Mickley, L., and Jacob, D.: General circulation model assessment of direct radiative forcing by the sulfate-nitrate-ammonium-water inorganic aerosol system, J Geophys Res-Atmos, 106, 1097–1111, https://doi.org/10.1029/2000JD900512, 2001.

Bauduin, S., Clarisse, L., Theunissen, M., George, M., Hurtmans, D., Clerbaux, C., and Coheur, P.-F.: IASI's sensitivity to near-surface carbon monoxide (CO): Theoretical analyses and retrievals on test cases, J. Quant. Spectrosc. Radiat. Transf., 189, 428–440, https://doi.org/10.1016/j.jqsrt.2016.12.022, 2017.

Beer, R., Shephard, M. W., Kulawik, S. S., Clough, S. A., Eldering, A., Bowman, K. W., Sander, S. P., Fisher, B. M., Payne, V. H., Luo, M., Osterman, G. B., and Worden, J. R.: First satellite observations of lower tropospheric ammonia and methanol, Geophys. Res. Lett., 35, 2008GL033642, https://doi.org/10.1029/2008GL033642, 2008.

Behera, S. N., Sharma, M., Aneja, V. P., and Balasubramanian, R.: Ammonia in the atmosphere: a review on emission sources, atmospheric chemistry and deposition on terrestrial bodies, Environ. Sci. Pollut. Res., 20, 8092–8131, https://doi.org/10.1007/s11356-013-2051-9, 2013.

Boynard, A., Clerbaux, C., Clarisse, L., Safieddine, S., Pommier, M., Van Damme, M., Bauduin, S., Oudot, C., Hadji-Lazaro, J., Hurtmans, D., and Coheur, P.: First simultaneous space measurements of atmospheric pollutants in the boundary layer from IASI: A case study in the North China Plain, Geophys. Res. Lett., 41, 645–651, https://doi.org/10.1002/2013GL058333, 2014.

Clarisse, L., Clerbaux, C., Dentener, F., Hurtmans, D., and Coheur, P.-F.: Global ammonia distribution derived from infrared satellite observations, Nat. Geosci., 2, 479–483, https://doi.org/10.1038/ngeo551, 2009.

Clarisse, L., Shephard, M. W., Dentener, F., Hurtmans, D., Cady-Pereira, K., Karagulian, F., Van Damme, M., Clerbaux, C., and Coheur, P.: Satellite monitoring of ammonia: A case study of the San Joaquin Valley, J. Geophys. Res. Atmospheres, 115, 2009JD013291, https://doi.org/10.1029/2009JD013291, 2010.

Clarisse, L., Clerbaux, C., Franco, B., Hadji-Lazaro, J., Whitburn, S., Kopp, A. K., Hurtmans, D., and Coheur, P. -F.: A Decadal Data Set of Global Atmospheric Dust Retrieved From IASI Satellite Measurements, J. Geophys. Res. Atmospheres, 124, 1618–1647, https://doi.org/10.1029/2018JD029701, 2019.

Clarisse, L., Van Damme, M., Hurtmans, D., Franco, B., Clerbaux, C., and Coheur, P.: The Diel Cycle of NH_3 Observed From the FY-4A Geostationary Interferometric Infrared Sounder (GIIRS), Geophys. Res. Lett., 48, e2021GL093010, https://doi.org/10.1029/2021GL093010, 2021.

Dammers, E., Schaap, M., Haaima, M., Palm, M., Wichink Kruit, R. J., Volten, H., Hensen, A., Swart, D., and Erisman, J. W.: Measuring atmospheric ammonia with remote sensing campaign: Part 1 – Characterisation of vertical ammonia concentration profile in the centre of The Netherlands, Atmos. Environ., 169, 97–112, https://doi.org/10.1016/j.atmosenv.2017.08.067, 2017.

De Mazière, M., Thompson, A. M., Kurylo, M. J., Wild, J. D., Bernhard, G., Blumenstock, T., Braathen, G. O., Hannigan, J. W., Lambert, J.-C., Leblanc, T., McGee, T. J., Nedoluha, G., Petropavlovskikh, I., Seckmeyer, G., Simon, P. C., Steinbrecht, W., and Strahan, S. E.: The Network for the Detection of Atmospheric Composition Change (NDACC): history, status and perspectives, Atmospheric Chem. Phys., 18, 4935–4964, https://doi.org/10.5194/acp-18-4935-2018, 2018.

Ding, J., Van Der A, R., Eskes, H., Dammers, E., Shephard, M., Wichink Kruit, R., Guevara, M., and Tarrason, L.: Ammonia emission estimates using CrIS satellite observations over Europe, Atmospheric Chem. Phys., 24, 10583–10599, https://doi.org/10.5194/acp-24-10583-2024, 2024.

Erisman, J. W., Sutton, M. A., Galloway, J., Klimont, Z., and Winiwarter, W.: How a century of ammonia synthesis changed the world, Nat. Geosci., 1, 636–639, https://doi.org/10.1038/ngeo325, 2008.

Erisman, J. W., Galloway, J. N., Seitzinger, S., Bleeker, A., Dise, N. B., Petrescu, A. M. R., Leach, A. M., and De Vries, W.: Consequences of human modification of the global nitrogen cycle, Philos. Trans. R. Soc. B Biol. Sci., 368, 20130116, https://doi.org/10.1098/rstb.2013.0116, 2013.

Ernst, J. W. and Massey, H. F.: The Effects of Several Factors on Volatilization of Ammonia Formed from Urea in the Soil, Soil Sci. Soc. Am. J., 24, 87–90, https://doi.org/10.2136/sssaj1960.03615995002400020007x, 1960.

Fowler, D., Coyle, M., Skiba, U., Sutton, M. A., Cape, J. N., Reis, S., Sheppard, L. J., Jenkins, A., Grizzetti, B., Galloway, J. N., Vitousek, P., Leach, A., Bouwman, A. F., Butterbach-Bahl, K., Dentener, F., Stevenson, D., Amann, M., and Voss, M.: The global nitrogen cycle in the twenty-first century, Philos. Trans. R. Soc. B Biol. Sci., 368, 20130164, https://doi.org/10.1098/rstb.2013.0164, 2013.

Galloway, J. N., Aber, J. D., Erisman, J. W., Seitzinger, S. P., Howarth, R. W., Cowling, E. B., and Cosby, B. J.: The Nitrogen Cascade, BioScience, 53, 341, https://doi.org/10.1641/0006-3568(2003)053%5B0341:TNC%5D2.0.CO;2, 2003.

Galloway, J. N., Dentener, F. J., Capone, D. G., Boyer, E. W., Howarth, R. W., Seitzinger, S. P., Asner, G. P., Cleveland, C. C., Green, P. A., Holland, E. A., Karl, D. M., Michaels, A. F., Porter, J. H., Townsend, A. R., and Vorosmarty, C. J.: Nitrogen Cycles: Past, Present, and Future, Biogeochemistry, 70, 153–226, https://doi.org/10.1007/s10533-004-0370-0, 2004.

Guendouz, N., Viatte, C., Zeng, Z., Boynard, A., Safieddine, S., Standfuss, C., Turquety, S., Van Damme, M., Clarisse, L., Coheur, P., Sheng, M., Armante, R., Prunet, P., and Clerbaux, C.: Monitoring Atmospheric Ammonia From Geostationary Orbit: Contributions of GIIRS-B and IRS Remote Sensors, J. Geophys. Res. Atmospheres, 131, e2025JD046139, https://doi.org/10.1029/2025JD046139, 2026.

Guo, H., Otjes, R., Schlag, P., Kiendler-Scharr, A., Nenes, A., and Weber, R. J.: Effectiveness of ammonia reduction on control of fine particle nitrate, Atmospheric Chem. Phys., 18, 12241–12256, https://doi.org/10.5194/acp-18-12241-2018, 2018.

Hempel, S., Saha, C. K., Fiedler, M., Berg, W., Hansen, C., Amon, B., and Amon, T.: Non-linear temperature dependency of ammonia and methane emissions from a naturally ventilated dairy barn, Biosyst. Eng., 145, 10–21, https://doi.org/10.1016/j.biosystemseng.2016.02.006, 2016.

Holmlund, K., Grandell, J., Schmetz, J., Stuhlmann, R., Bojkov, B., Munro, R., Lekouara, M., Coppens, D., Viticchie, B., August, T., Theodore, B., Watts, P., Dobber, M., Fowler, G., Bojinski, S., Schmid, A., Salonen, K., Tjemkes, S., Aminou, D., and Blythe, P.: Meteosat Third Generation (MTG): Continuation and Innovation of Observations from Geostationary Orbit, Bull. Am. Meteorol. Soc., 102, E990–E1015, https://doi.org/10.1175/BAMS-D-19-0304.1, 2021.

Hua, J., Liu, S., Qi, C., Wu, S., Lee, L., Hu, X., Zhao, X., Strong, K., Flood, V., Franco, B., Clarisse, L., Clerbaux, C., Wunch, D., Roehl, C., Wennberg, P., and Zeng, Z.-C.: Observing carbon monoxide and volatile organic compounds from Canadian wildfires in 2023 from FengYun-3E/HIRAS-II in a dawn-dusk sun-synchronous orbit, Remote Sens. Environ., 327, 114829, https://doi.org/10.1016/j.rse.2025.114829, 2025.

Isaksen, I. S. A., Granier, C., Myhre, G., Berntsen, T. K., Dalsøren, S. B., Gauss, M., Klimont, Z., Benestad, R., Bousquet, P., Collins, W., Cox, T., Eyring, V., Fowler, D., Fuzzi, S., Jöckel, P., Laj, P., Lohmann, U., Maione, M., Monks, P., Prevot, A. S.

H., Raes, F., Richter, A., Rognerud, B., Schulz, M., Shindell, D., Stevenson, D. S., Storelvmo, T., Wang, W.-C., Van Weele, M., Wild, M., and Wuebbles, D.: Atmospheric composition change: Climate–Chemistry interactions, Atmos. Environ., 43, 5138–5192, https://doi.org/10.1016/j.atmosenv.2009.08.003, 2009.

Jiménez, E., Cabañas, B., and Lefebvre, G. (Eds.): Environment, Energy and Climate Change I: Environmental Chemistry of Pollutants and Wastes, Springer International Publishing, Cham, https://doi.org/10.1007/978-3-319-12907-5, 2015.

Kuang, Y., Xu, W., Lin, W., Meng, Z., Zhao, H., Ren, S., Zhang, G., Liang, L., and Xu, X.: Explosive morning growth phenomena of NH3 on the North China Plain: Causes and potential impacts on aerosol formation, Environ. Pollut., 257, 113621, https://doi.org/10.1016/j.envpol.2019.113621, 2020.

Li, Z., Sun, K., Guan, K., Wang, S., Peng, B., Clarisse, L., Van Damme, M., Coheur, P.-F., Cady-Pereira, K., Shephard, M. W., Zondlo, M., and Moore, D.: Ammonia emissions and depositions over the contiguous United States derived from IASI and CrIS using the directional derivative approach, https://doi.org/10.5194/egusphere-2025-725, 5 March 2025.

Lindaas, J., Pollack, I. B., Calahorrano, J. J., O'Dell, K., Garofalo, L. A., Pothier, M. A., Farmer, D. K., Kreidenweis, S. M., Campos, T., Flocke, F., Weinheimer, A. J., Montzka, D. D., Tyndall, G. S., Apel, E. C., Hills, A. J., Hornbrook, R. S., Palm, B. B., Peng, Q., Thornton, J. A., Permar, W., Wielgasz, C., Hu, L., Pierce, J. R., Collett, J. L., Sullivan, A. P., and Fischer, E. V.: Empirical Insights Into the Fate of Ammonia in Western U.S. Wildfire Smoke Plumes, J. Geophys. Res. Atmospheres, 126, e2020JD033730, https://doi.org/10.1029/2020JD033730, 2021.

Liu, M., Huang, X., Song, Y., Xu, T., Wang, S., Wu, Z., Hu, M., Zhang, L., Zhang, Q., Pan, Y., Liu, X., and Zhu, T.: Rapid SO_2 emission reductions significantly increase tropospheric ammonia concentrations over the North China Plain, Atmospheric Chem. Phys., 18, 17933–17943, https://doi.org/10.5194/acp-18-17933-2018, 2018.

Liu, X., Zhang, Y., Han, W., Tang, A., Shen, J., Cui, Z., Vitousek, P., Erisman, J. W., Goulding, K., Christie, P., Fangmeier, A., and Zhang, F.: Enhanced nitrogen deposition over China, Nature, 494, 459–462, https://doi.org/10.1038/nature11917, 2013.

Lonsdale, C. R., Hegarty, J. D., Cady-Pereira, K. E., Alvarado, M. J., Henze, D. K., Turner, M. D., Capps, S. L., Nowak, J. B., Neuman, J. A., Middlebrook, A. M., Bahreini, R., Murphy, J. G., Markovic, M. Z., VandenBoer, T. C., Russell, L. M., and Scarino, A. J.: Modeling the diurnal variability of agricultural ammonia in Bakersfield, California, during the CalNex campaign, Atmospheric Chem. Phys., 17, 2721–2739, https://doi.org/10.5194/acp-17-2721-2017, 2017.

Luo, Z., Zhang, Y., Chen, W., Van Damme, M., Coheur, P.-F., and Clarisse, L.: Estimating global ammonia (NH_3) emissions based on IASI observations from 2008 to 2018, Atmospheric Chem. Phys., 22, 10375–10388, https://doi.org/10.5194/acp-22-10375-2022, 2022.

Lutsch, E., Strong, K., Jones, D. B. A., Ortega, I., Hannigan, J. W., Dammers, E., Shephard, M. W., Morris, E., Murphy, K., Evans, M. J., Parrington, M., Whitburn, S., Van Damme, M., Clarisse, L., Coheur, P., Clerbaux, C., Croft, B., Martin, R. V., Pierce, J. R., and Fisher, J. A.: Unprecedented Atmospheric Ammonia Concentrations Detected in the High Arctic From the 2017 Canadian Wildfires, J. Geophys. Res. Atmospheres, 124, 8178–8202, https://doi.org/10.1029/2019JD030419, 2019.

Myhre, G., Samset, B. H., Schulz, M., Balkanski, Y., Bauer, S., Berntsen, T. K., Bian, H., Bellouin, N., Chin, M., Diehl, T., Easter, R. C., Feichter, J., Ghan, S. J., Hauglustaine, D., Iversen, T., Kinne, S., Kirkevåg, A., Lamarque, J.-F., Lin, G., Liu, X., Lund, M. T., Luo, G., Ma, X., Van Noije, T., Penner, J. E., Rasch, P. J., Ruiz, A., Seland, Ø., Skeie, R. B., Stier, P., Takemura, T., Tsigaridis, K., Wang, P., Wang, Z., Xu, L., Yu, H., Yu, F., Yoon, J.-H., Zhang, K., Zhang, H., and Zhou, C.: Radiative forcing of the direct aerosol effect from AeroCom Phase II simulations, Atmospheric Chem. Phys., 13, 1853–1877, https://doi.org/10.5194/acp-13-1853-2013, 2013.

Perrone, D.: Groundwater Overreliance Leaves Farmers and Households High and Dry, One Earth, 2, 214–217, https://doi.org/10.1016/j.oneear.2020.03.001, 2020.

Saraswati, Sharma, S. K., and Mandal, T. K.: Five-year measurements of ambient ammonia and its relationships with other trace gases at an urban site of Delhi, India, Meteorol. Atmospheric Phys., 130, 241–257, https://doi.org/10.1007/s00703-017-0512-2, 2018.

Saylor, R. D., Edgerton, E. S., Hartsell, B. E., Baumann, K., and Hansen, D. A.: Continuous gaseous and total ammonia measurements from the southeastern aerosol research and characterization (SEARCH) study, Atmos. Environ., 44, 4994–5004, https://doi.org/10.1016/j.atmosenv.2010.07.055, 2010.

Schjoerring, J. K., Husted, S., and Mattsson, M.: Physiological parameters controlling plant–atmosphere ammonia exchange, Atmos. Environ., 32, 491–498, https://doi.org/10.1016/S1352-2310(97)00006-X, 1998.

Sheng, M., Zhou, R., Hua, J., Han, S., Zhang, L., Wang, W., Dang, R., Cao, H., Chen, Z., Gu, Y., Liu, M., Lee, L., Qi, C., Han, C., Shephard, M. W., Guendouz, N., Viatte, C., Clarisse, L., Van Damme, M., Clerbaux, C., and Zeng, Z.-C.: Geostationary observations of atmospheric ammonia over East Asia: spatio-temporal variations revealed by three years of FY-4B/GIIRS measurements, https://doi.org/10.5194/egusphere-2025-5699, 25 November 2025.

Shephard, M. W. and Cady-Pereira, K. E.: Cross-track Infrared Sounder (CrIS) satellite observations of tropospheric ammonia, Atmospheric Meas. Tech., 8, 1323–1336, https://doi.org/10.5194/amt-8-1323-2015, 2015.

Shephard, M. W., Cady-Pereira, K. E., Luo, M., Henze, D. K., Pinder, R. W., Walker, J. T., Rinsland, C. P., Bash, J. O., Zhu, L., Payne, V. H., and Clarisse, L.: TES ammonia retrieval strategy and global observations of the spatial and seasonal variability of ammonia, Atmospheric Chem. Phys., 11, 10743–10763, https://doi.org/10.5194/acp-11-10743-2011, 2011.

Shephard, M. W., Dammers, E., Cady-Pereira, K. E., Kharol, S. K., Thompson, J., Gainariu-Matz, Y., Zhang, J., McLinden, C. A., Kovachik, A., Moran, M., Bittman, S., Sioris, C. E., Griffin, D., Alvarado, M. J., Lonsdale, C., Savic-Jovcic, V., and Zheng, Q.: Ammonia measurements from space with the Cross-track Infrared Sounder: characteristics and applications, Atmospheric Chem. Phys., 20, 2277–2302, https://doi.org/10.5194/acp-20-2277-2020, 2020.

Someya, Y., Imasu, R., Shiomi, K., and Saitoh, N.: Atmospheric ammonia retrieval from the TANSO-FTS/GOSAT thermal infrared sounder, Atmospheric Meas. Tech., 13, 309–321, https://doi.org/10.5194/amt-13-309-2020, 2020.

Sutton, A. D., Burrell, A. K., Dixon, D. A., Garner, E. B., Gordon, J. C., Nakagawa, T., Ott, K. C., Robinson, J. P., and Vasiliu, M.: Regeneration of Ammonia Borane Spent Fuel by Direct Reaction with Hydrazine and Liquid Ammonia, Science, 331, 1426–1429, https://doi.org/10.1126/science.1199003, 2011.

Sutton, M. A., Reis, S., Riddick, S. N., Dragosits, U., Nemitz, E., Theobald, M. R., Tang, Y. S., Braban, C. F., Vieno, M., Dore, A. J., Mitchell, R. F., Wanless, S., Daunt, F., Fowler, D., Blackall, T. D., Milford, C., Flechard, C. R., Loubet, B., Massad, R., Cellier, P., Personne, E., Coheur, P. F., Clarisse, L., Van Damme, M., Ngadi, Y., Clerbaux, C., Skjøth, C. A., Geels, C., Hertel, O., Wichink Kruit, R. J., Pinder, R. W., Bash, J. O., Walker, J. T., Simpson, D., Horváth, L., Misselbrook, T. H., Bleeker, A., Dentener, F., and De Vries, W.: Towards a climate-dependent paradigm of ammonia emission and deposition, Philos. Trans. R. Soc. B Biol. Sci., 368, 20130166, https://doi.org/10.1098/rstb.2013.0166, 2013.

Tevlin, A. G., Li, Y., Collett, J. L., McDuffie, E. E., Fischer, E. V., and Murphy, J. G.: Tall Tower Vertical Profiles and Diurnal Trends of Ammonia in the Colorado Front Range, J. Geophys. Res. Atmospheres, 122, https://doi.org/10.1002/2017JD026534, 2017.

Van Damme, M., Erisman, J. W., Clarisse, L., Dammers, E., Whitburn, S., Clerbaux, C., Dolman, A. J., and Coheur, P.-F.: Worldwide spatiotemporal atmospheric ammonia (NH_3) columns variability revealed by satellite, Geophys. Res. Lett., 42, 8660–8668, https://doi.org/10.1002/2015GL065496, 2015.

Walker, J. T., Robarge, W. P., Wu, Y., and Meyers, T. P.: Measurement of bi-directional ammonia fluxes over soybean using the modified Bowen-ratio technique, Agric. For. Meteorol., 138, 54–68, https://doi.org/10.1016/j.agrformet.2006.03.011, 2006.

Wang, Q., Zhang, Q., Ma, Z., Ge, B., Xie, C., Zhou, W., Zhao, J., Xu, W., Du, W., Fu, P., Lee, J., Nemitz, E., Cowan, N., Mullinger, N., Cheng, X., Zhou, L., Yue, S., Wang, Z., and Sun, Y.: Temporal characteristics and vertical distribution of atmospheric ammonia and ammonium in winter in Beijing, Sci. Total Environ., 681, 226–234, https://doi.org/10.1016/j.scitotenv.2019.05.137, 2019.

Wang, T., Song, Y., Xu, Z., Liu, M., Xu, T., Liao, W., Yin, L., Cai, X., Kang, L., Zhang, H., and Zhu, T.: Why is the Indo-Gangetic Plain the region with the largest NH_3 column in the globe during pre-monsoon and monsoon seasons?, Atmospheric Chem. Phys., 20, 8727–8736, https://doi.org/10.5194/acp-20-8727-2020, 2020.

Wang, W., Liu, C., Clarisse, L., Van Damme, M., Coheur, P.-F., Xie, Y., Shan, C., Hu, Q., Sun, Y., and Jones, N.: Ground-based measurements of atmospheric NH_3 by Fourier transform infrared spectrometry at Hefei and comparisons with IASI data, Atmos. Environ., 287, 119256, https://doi.org/10.1016/j.atmosenv.2022.119256, 2022.

Warner, J. X., Wei, Z., Strow, L. L., Dickerson, R. R., and Nowak, J. B.: The global tropospheric ammonia distribution as seen in the 13-year AIRS measurement record, Atmospheric Chem. Phys., 16, 5467–5479, https://doi.org/10.5194/acp-16-5467-2016, 2016.

Warner, J. X., Dickerson, R. R., Wei, Z., Strow, L. L., Wang, Y., and Liang, Q.: Increased atmospheric ammonia over the world's major agricultural areas detected from space, Geophys. Res. Lett., 44, 2875–2884, https://doi.org/10.1002/2016GL072305, 2017.

Weber, R. J., Guo, H., Russell, A. G., and Nenes, A.: High aerosol acidity despite declining atmospheric sulfate concentrations over the past 15 years, Nat. Geosci., 9, 282–285, https://doi.org/10.1038/ngeo2665, 2016.

Wells, K. C., Millet, D. B., Payne, V. H., Deventer, M. J., Bates, K. H., De Gouw, J. A., Graus, M., Warneke, C., Wisthaler, A., and Fuentes, J. D.: Satellite isoprene retrievals constrain emissions and atmospheric oxidation, Nature, 585, 225–233, https://doi.org/10.1038/s41586-020-2664-3, 2020.

Wells, K. C., Millet, D. B., Payne, V. H., Vigouroux, C., Aquino, C. A. B., De Mazière, M., De Gouw, J. A., Graus, M., Kurosu, T., Warneke, C., and Wisthaler, A.: Next-Generation Isoprene Measurements From Space: Detecting Daily Variability at High Resolution, J. Geophys. Res. Atmospheres, 127, e2021JD036181, https://doi.org/10.1029/2021JD036181, 2022.

Zavyalov, V., Esplin, M., Scott, D., Esplin, B., Bingham, G., Hoffman, E., Lietzke, C., Predina, J., Frain, R., Suwinski, L., Han, Y., Major, C., Graham, B., and Phillips, L.: Noise performance of the CrIS instrument, J. Geophys. Res. Atmospheres, 118, https://doi.org/10.1002/2013JD020457, 2013.

Zeng, Z.-C.: Global carbon monoxide retrieval from the hyperspectral infrared atmospheric sounder-II onboard FengYun-3E in a dawn-dusk sun-synchronous orbit, J. Quant. Spectrosc. Radiat. Transf., 333, 109336, https://doi.org/10.1016/j.jqsrt.2024.109336, 2025.

Zeng, Z.-C., Lee, L., Qi, C., Clarisse, L., and Van Damme, M.: Optimal estimation retrieval of tropospheric ammonia from the Geostationary Interferometric Infrared Sounder on board FengYun-4B, Atmospheric Meas. Tech., 16, 3693–3713, https://doi.org/10.5194/amt-16-3693-2023, 2023.

Zeng, Z.-C., Clarisse, L., Franco, B., Clerbaux, C., Theys, N., Qi, C., Lee, L., Zhu, L., Hu, X., Gu, M., and Zhang, P.: Volcanic sulfur dioxide monitored from a constellation of FengYun hyperspectral infrared sounders in dawn-dusk, mid-morning, and afternoon sun-synchronous orbits, Remote Sens. Environ., 331, 115057, https://doi.org/10.1016/j.rse.2025.115057, 2025.

Zhan, X., Adalibieke, W., Cui, X., Winiwarter, W., Reis, S., Zhang, L., Bai, Z., Wang, Q., Huang, W., and Zhou, F.: Improved Estimates of Ammonia Emissions from Global Croplands, Environ. Sci. Technol., 55, 1329–1338, https://doi.org/10.1021/acs.est.0c05149, 2021.

Zhang, C., Qi, C., Yang, T., Gu, M., Zhang, P., Lee, L., Xie, M., and Hu, X.: Evaluation of FY-3E/HIRAS-II Radiometric Calibration Accuracy Based on OMB Analysis, Remote Sens., 14, 3222, https://doi.org/10.3390/rs14133222, 2022a.

Zhang, L., Chen, Y., Zhao, Y., Henze, D. K., Zhu, L., Song, Y., Paulot, F., Liu, X., Pan, Y., Lin, Y., and Huang, B.: Agricultural ammonia emissions in China: reconciling bottom-up and top-down estimates, Atmospheric Chem. Phys., 18, 339–355, https://doi.org/10.5194/acp-18-339-2018, 2018.

Zhang, P., Hu, X., Lu, Q., Zhu, A., Lin, M., Sun, L., Chen, L., and Xu, N.: FY-3E: The First Operational Meteorological Satellite Mission in an Early Morning Orbit, Adv. Atmospheric Sci., 39, 1–8, https://doi.org/10.1007/s00376-021-1304-7, 2022b.

Zhang, P., Hu, X., Sun, L., Xu, N., Chen, L., Zhu, A., Lin, M., Lu, Q., Yang, Z., Yang, J., and Wang, J.: The On-Orbit Performance of FY-3E in an Early Morning Orbit, Bull. Am. Meteorol. Soc., 105, E144–E175, https://doi.org/10.1175/BAMS-D-22-0045.1, 2024.

Zhang, Y., Dore, A. J., Ma, L., Liu, X. J., Ma, W. Q., Cape, J. N., and Zhang, F. S.: Agricultural ammonia emissions inventory and spatial distribution in the North China Plain, Environ. Pollut., 158, 490–501, https://doi.org/10.1016/j.envpol.2009.08.033, 2010.

Zhou, M., Deng, Z., Robert, C., Zhang, X., Zhang, L., Wang, Y., Qi, C., Wang, P., and Mazière, M. D.: The First Global Map of Atmospheric Ammonia (NH_3) as Observed by the HIRAS/FY-3D Satellite, Adv. Atmospheric Sci., 41, 379–390, https://doi.org/10.1007/s00376-023-3059-9, 2024.